nature chemical biology

Article

https://doi.org/10.1038/s41589-026-02269-z

Computational design of antimicrobial peptide nanopores

Received: 26 September 2025

Accepted: 10 June 2026

Published online: 03 August 2026

Check for updates

Rahul Deb[1,2,3], Marcelo D. T. Torres[4,5,6,7,8], Ivo Kabelka[1], Jan Přibyl[1], Kateřina Dvořáková Bendová[9], Edo Vreeker[10], Markéta Koběrská[11], Gabriela Balíková Novotná[11], Miloš Petřík[9,12,13], Giovanni Maglia[10], Cesar de la Fuente-Nunez[4,5,6,7,8] & Robert Vácha[1,2,14]

Antibiotic resistance is a global health threat, driving the need for new molecules that kill bacteria via nontraditional mechanisms. Here, we present a computational de novo design strategy for α-helical peptides that self-assemble into large, stable and membrane-spanning nanopores with antimicrobial activity, including in vivo efficacy against drug-resistant pathogens. Molecular dynamics simulations guided the selection of sequences for transmembrane barrel-stave pore formation, which were validated by microscopy, electrophysiology and fluorescence assays. Using computational and experimental analyses, including negative design controls, we developed general design guidelines and 52 modular sequence templates with tunable antimicrobial, pore-forming properties. Mechanistic studies confirmed bacterial cytoplasmic membrane disruption via designed nanopore formation. A tuned lead peptide selectively killed drug-resistant ESKAPEE bacteria, including *Acinetobacter baumannii*, without harming human cells, and showed anti-infective efficacy in preclinical mouse infection models. The framework presented here enables the design of synthetic peptide nanopores for precision antimicrobials, anticancer agents, molecular sensors and delivery systems.

The de novo design of peptide sequences that fold and assemble into defined structures with tailored functions is a stringent test of our understanding of peptide self-assembly and a gateway to engineering next-generation therapeutics and biomolecular machines. Among such constructs, short synthetic peptides that self-assemble into transmembrane barrel-stave pores (TBPs) can modulate membrane permeability with high precision[1,2]. These peptides form barrel-shaped bundles that span lipid bilayers and contain nanometer-sized central pores that permit the transport of small molecules across membranes (Fig. 1a). TBPs hold promise for applications in biotechnology and medicine[3,4], particularly as scaffolds for antimicrobial peptides (AMPs)[5–7]. TBP-forming AMPs can rapidly kill bacteria by disrupting membrane integrity[8], and bacterial resistance to such mechanisms typically evolves slowly[5,6,9,10], making them potential candidates for next-generation antibiotics[10]. Despite the discovery of thousands of AMPs[11], few have been shown to form a TBP structure, including alamethicin[12,13]. This study establishes a modular computational framework for the de novo design of TBP-forming peptides with tunable antimicrobial activity.

Designing TBP-forming peptides de novo is challenging due to the complex interplay of peptide–peptide, peptide–membrane and peptide–solvent interactions that govern pore formation and stability[14,15]. These assemblies are highly sensitive to sequence-level variation (even single-residue mutations can disrupt pore assembly or function)[8,16]. A few α-helical peptide structures resembling TBPs have been designed, including $(LSSLLSL)_3$ (ref. 1), the Zn^{2+}/H^+ antiporter[17], coiled-coils[18], engineered narrow ion channels[19–23] and double-barrel pores[24], but none exhibit antimicrobial activity. Generalizable design principles remain elusive, as residue-level contributions to assembly and function are often unknown or context dependent[25]. Experimental techniques for resolving these interactions require high-resolution probing of

A full list of affiliations appears at the end of the paper. e-mail: robert.vacha@muni.cz

https://doi.org/10.1038/s41589-026-02269-z

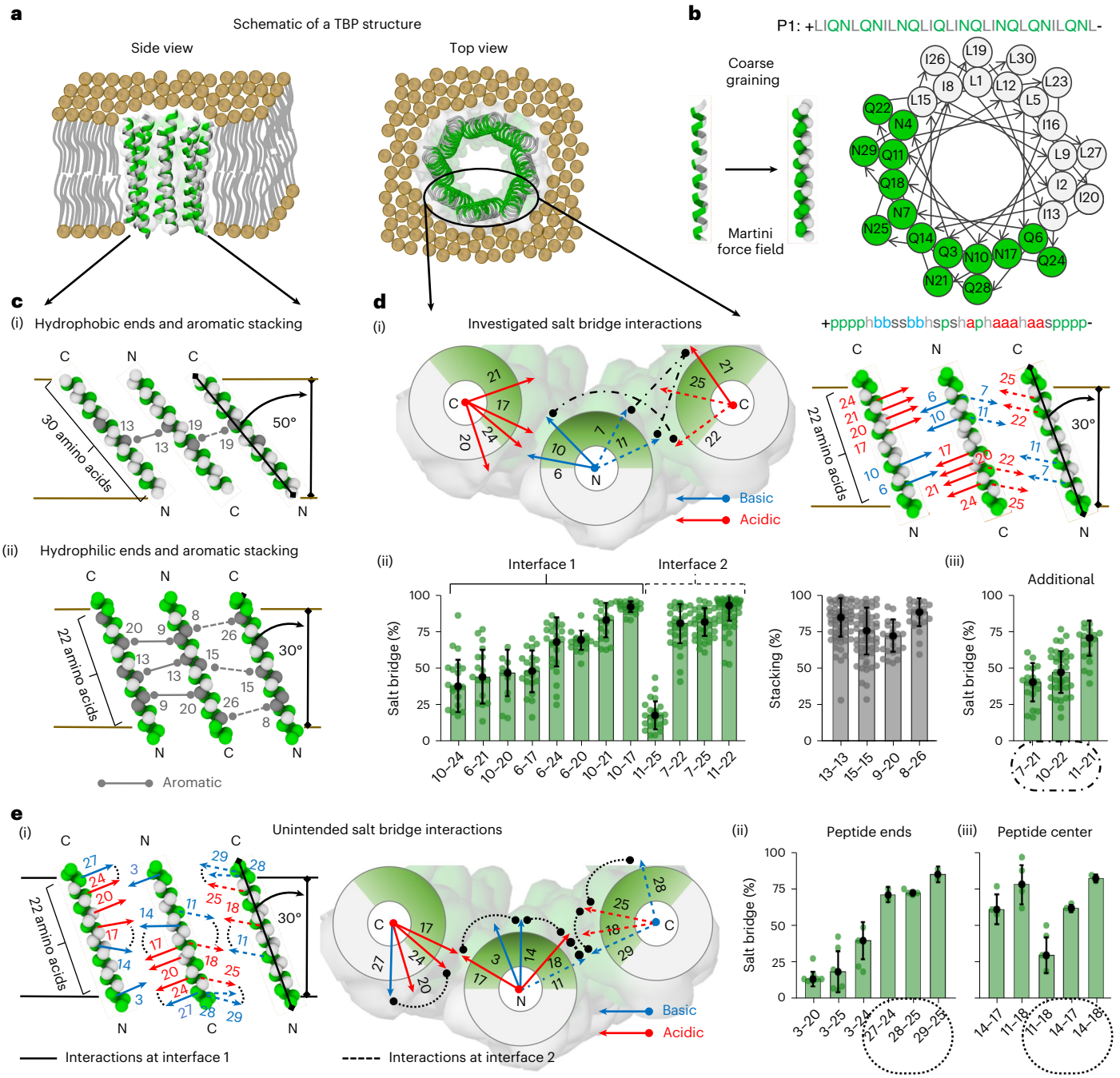

Fig. 1 | Rational optimization of aromatic stacking and salt bridge interactions stabilizing TBPs. a, Schematic of an octameric, α-helical TBP. **b**, Sequence, helical wheel and all-atom-to-coarse-grained conversion of 30-residue amphipathic peptide P1 (Supplementary Table 1). **c**, Schematic of aromatic stacking interactions for peptides with a continuous hydrophobic patch spanning 30 amino acids (i) and 22 amino acids (ii). **d**, Schematic of salt bridge interactions; sequence pattern: polar (p: glutamine/asparagine), hydrophobic (h: leucine/isoleucine), basic (b: arginine), acidic (a: aspartic acid) and aromatic (s: tryptophan/phenylalanine). Basic/acidic and aromatic positions can be substituted with polar and hydrophobic residues, respectively (i). The stability of designed interactions (ii) and additional salt bridges between neighboring peptide–peptide interfaces (iii) are shown. **e**, Schematic (i) and stability of unintended inter- and intramolecular salt bridges at the peptide ends (ii) and peptide center (iii). Schematics are shown for three antiparallel transmembrane peptides (tilted 50°/30°) representing two neighboring interfaces. Each point represents the mean designed contact percentage over 51 µs of simulation time ± s.d., derived from at least three independent simulations for each designed interaction contact. Simulations were performed using a POPC lipid membrane. Color code in schematics: peptide hydrophilic backbone/residues, green; peptide hydrophobic backbone/residues, white; aromatic residues, silver.

metastable nanostructures[2], whereas molecular simulations offer atomic-scale insights into peptide assembly and function[8,16,26].

Here, we report a modular, computational de novo design framework for α-helical AMPs that assemble into membrane-spanning TBPs. Molecular dynamics (MD) simulations revealed residue-specific contributions to pore formation, guiding the design of peptides, which were then validated through microscopy, electrophysiology, fluorescence, microdilution and membrane permeabilization assays. Tuned peptides selectively killed multidrug-resistant ESKAPEE pathogens without harming human cells and showed anti-infective efficacy

without adverse effects in preclinical animal models. The results establish a generalizable strategy and introduce sequence libraries for engineering programmable peptide therapeutics and synthetic nanopores.

Results

Tailored design of TBPs

We developed a computational design strategy to identify residue-level contributions that stabilize TBPs. Using ~150 systematically varied amphipathic 30-residue α-helical peptides (a length required to span a 1-palmitoyl-2-oleoyl-*sn*-glycero-3-phosphocholine (POPC) lipid bilayer), we performed MD simulations with the coarse-grained Martini 2.2 force field[27] (Fig. 1b and Methods). Each system comprised a preformed membrane-embedded pore with eight transmembrane peptides in antiparallel arrangement, the preferred geometry for helix self-assembly[26,28,29]. Octameric TBPs were selected as the smallest nanopores capable of supporting small-molecule transport[19,21,24]. Unbiased simulations of 51 µs per peptide allowed us to assess pore stability via structural rearrangement. Pore stability varied with interaction strength and geometry, and was defined by the number of transmembrane peptides remaining at simulation end: stable pore (eight peptides), partially deformed pore (four to seven peptides) or fully closed pore (less than four peptides). Stable TBPs were assumed to be low-energy states that could form spontaneously after overcoming kinetic barriers[14,15]. Spontaneous pore formation was investigated in a separate set of simulations.

Role of aromatic and terminal interactions in pore stabilization

Close packing of hydrophobic and aromatic side chains (via knobs-into-holes interactions[18,22,25] and π–π stacking[17,30,31]) is important in driving helix oligomerization, a process essential for TBP assembly. To evaluate the contribution of these interactions to TBP stability, we simulated peptides with varied hydrophobic residues (P1–P6; Supplementary Fig. 1a and Supplementary Table 1). Starting from an amphipathic sequence containing hydrophobic leucine/isoleucine and hydrophilic glutamine/asparagine, we found that varying hydrophobic content alone (23–77%) did not stabilize TBPs. However, replacing leucine/isoleucine with aromatic tryptophan and phenylalanine improved pore stability. A fully aromatic patch yielded a stable but narrow, water-impermeable pore (P6; Supplementary Fig. 1b). We next assessed how aromatic residue positioning influences interpeptide (intermolecular) stacking (P7–P15; Supplementary Table 1). Precise placement was found to be critical; residues too close on the same helix formed intramolecular π–π interactions that disrupted pore assembly (Supplementary Fig. 1c). For example, adding an extra tryptophan at position 16 induced intramolecular interactions that interfered with intermolecular stacking and closed the pore (P10). In peptides with 30-residue hydrophobic stretches, the helices tilted 50° relative to the membrane normal. With such a tilt, the optimal stacking positions were 13 and 19 (P14–P15; Fig. 1c(i) and Supplementary Fig. 1d), increasing pore stability, but they did not fully stabilize TBPs (Supplementary Fig. 1e,f). To assess the role of termini, we shortened the hydrophobic patch to 22 residues, added cationic arginine residues at the termini (NQRR- or RRQN-; P16–P17; Supplementary Table 1) and tested C-terminal amidation (-NH_2). These peptides formed deformed pores, whereas fully hydrophobic P1 collapsed. Together, these results indicated that terminal cationic residues, the N-terminal NH_3^+ and the C-terminal COO^- promote transmembrane helix stability and assembly via electrostatic and hydrogen bonding interactions[26,29]. Finally, we combined cationic termini with optimized aromatic stacking (P18–P27; Supplementary Table 1). With 22-residue hydrophobic stretches, peptides tilted 30°, reorienting helix packing geometry and shifting optimal stacking to residues 13 and 15 (single stacking) and 8, 9, 20 and 26 (double stacking) per interface (Fig. 1c(ii) and Supplementary Fig. 1g). Peptides with only single stacking formed deformed pores, whereas those with double stacking fully stabilized TBPs. Omission of cationic termini abolished stability. These findings reveal that synergistic tuning of aromatic stacking geometry and terminal charge distribution is crucial for TBP stabilization.

Design principles of salt bridge interactions in pore stabilization

Salt bridges between charged residues can enhance TBP stability[32]. To evaluate their contribution, we designed 75 peptides featuring arginine–aspartic acid salt bridges at feasible hydrophilic positions, using either single or double stacking per peptide–peptide interface (Supplementary Tables 2 and 3). Peptides were grouped by salt bridge density: A–B (two bridges per interface) and C–D (four bridges per interface; Supplementary Note 1). We investigated interfacial positions 6, 10, 17, 20, 21 and 24 (interface 1) and 7, 11, 22 and 25 (interface 2; Fig. 1d(i)). Pore stability increased with higher salt bridge density. Stabilizing efficiency, based on the frequency and duration of interactions, followed the following order (Fig. 1d(ii)): interface 1: 10–24 < 6–21 < 10–20 < 6–17 < 6–24 < 6–20 < 10–21 < 10–17; interface 2: 11–25 < 7–22 < 7–25 < 11–22. Unintended intermolecular salt bridges, such as 7–21, 10–22 and 11–21 (cross-interface; Fig. 1d(iii)) and 3–20, 3–24 and 3–25 (adjacent termini; Fig. 1e(i,ii)), further enhanced TBP stability. By contrast, intramolecular salt bridges (for example, 14–17 and 11–18 centrally; 27–24, 28–25 and 29–25 at the C terminus) disrupted key interactions, particularly 6–24 and 7–25 (Fig. 1e(i,iii)).

Peptides in groups C–D formed extended ladders of salt bridges (charge zippers[32]) across each interface (Fig. 1d(i)), yielding more compact and stable TBPs than in groups A–B. To test robustness, we tested 33 rationally designed mutations. (1) Cationic substitutions and added charges. We tested lysine substitutions and increased net charge for their ability to enhance selectivity for anionic bacterial membranes[5,6,33]. Arginine-to-lysine substitutions and cationic additions at termini or polar faces had minimal impact on salt bridge stability (Fig. 2a and Supplementary Table 4). However, in groups C–D, added charges formed unintended salt bridges (Fig. 1e(i,ii)), subtly perturbing the designed network. In group A, similar additions disrupted salt bridge geometry (Supplementary Table 5), indicating that excess charge must be introduced cautiously. (2) Swapping charge-pair orientations. Reversing the positions of charge pairs, that is, arginine–aspartic acid to aspartic acid–arginine, in group C preserved TBP stability (Fig. 2b(i,ii) and Supplementary Table 6). However, adding lysine residues at termini introduced unintended inter- (27–6, 28–6, 29–7, 29–10 and 29–11) and intramolecular (2–6, 3–6, 3–7 and 4–7) salt bridges (Fig. 2b(iii)), destabilizing designed pairs. (3) Sequence context and substitutions. To test (LIQN) sequence dependence, we replaced glutamine/asparagine and leucine/isoleucine with serine and valine (Fig. 2c and Supplementary Table 7). In groups C–D, serine–serine hydrogen bonding[34] narrowed the pore but maintained integrity. In groups A–B, however, stabilizing interactions were reduced, and pores frequently collapsed (Supplementary Fig. 2a–e). A chemically diverse group C variant (All C16 + 8), comprising all major amino acid types (threonine, glutamine, serine, asparagine, alanine, methionine, valine, leucine, isoleucine, tryptophan, phenylalanine, arginine, lysine, aspartic acid and glutamic acid; Supplementary Table 7), also formed a stable TBP (Supplementary Fig. 2f), illustrating the broad compatibility of the design strategy. (4) Without aromatic stacking. To test the pore-stabilizing effects of salt bridges alone, we additionally used a 'scaled' version of the Martini force field with reduced interaction strengths (see Methods), given that the standard Martini force field can overestimate binding free energies[35]. Groups A–B lost pore stability except for peptides containing the most robust salt bridges (6–20, 7–25, 10–17 and 11–22; Fig. 2d and Supplementary Table 8). However, these peptides could not stabilize pores without aromatic stacking (Fig. 2e, Supplementary Fig. 2g–j and Supplementary Table 9). By contrast, groups C–D retained pore stability even in the absence of stacking (Fig. 2e and Supplementary Fig. 2k–m). Together, these results

https://doi.org/10.1038/s41589-026-02269-z

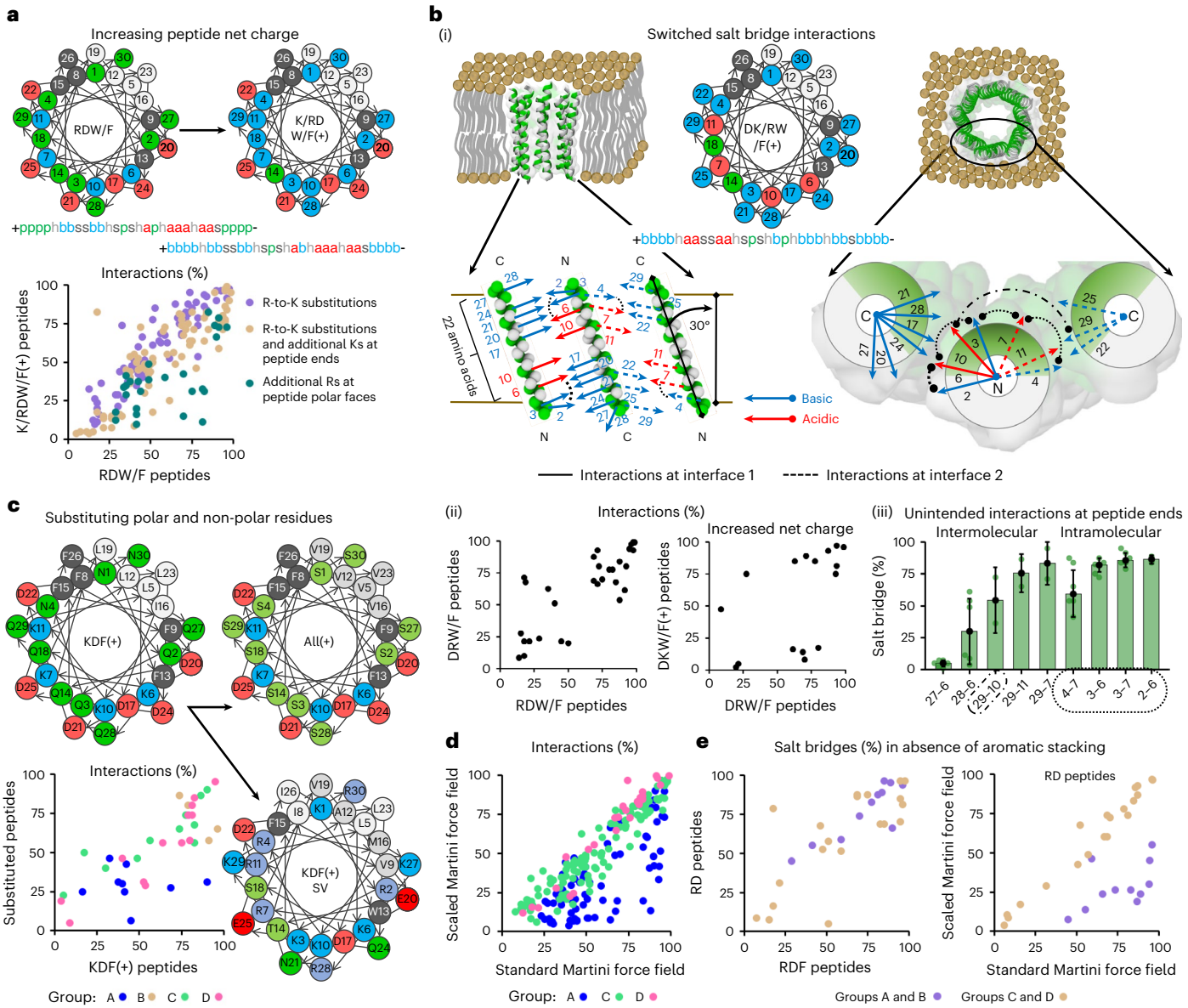

Fig. 2 | Charge zippers and robustness of TBPs with different mutations. **a**, Cationic substitutions and added charges: peptide helical wheels, sequence patterns and correlations between interaction strengths in simulations of RDW/F peptides and their charged variants (Supplementary Tables 4 and 5). **b**, Swapping charge-pair orientations. (i) Helical wheel, sequence pattern and schematic of salt bridge interactions between three antiparallel transmembrane peptides (representing two neighboring peptide–peptide interfaces). Sequence pattern: polar (p: glutamine/asparagine), hydrophobic (h: leucine/isoleucine), basic (b: arginine/lysine), acidic (a: aspartic acid) and aromatic (s: tryptophan/phenylalanine); basic/acidic and aromatic sites may be replaced with polar and hydrophobic residues, respectively. (ii) Correlation for RDW/F peptides and their DRW/F variants, including those with higher net charge. (iii) Stability of unintended inter- (for example, 29–10, dot-dash) and intramolecular (dotted) salt bridges (Supplementary Table 6). Data are presented as the mean designed contact percentage over 51 µs of simulation time ± s.d., derived from at least three independent simulations for each designed interaction contact. **c**, Sequence context and substitutions: helical wheels and correlations for KDF peptides and their variants (Supplementary Table 7). **d**,**e**, Correlations using standard versus scaled Martini force fields for RDW/F peptides (**d**; Supplementary Tables 2 and 8) and RD peptides (**e**) without aromatic stacking (Supplementary Table 9). Each point represents the mean designed contact percentage over 51 µs of simulation time, derived from at least three independent simulations for each designed interaction contact. Simulations were performed using a POPC lipid membrane. Color code in schematics: peptide hydrophilic backbone/residues, green; peptide hydrophobic backbone/residues, white; aromatic residues, silver; basic residues, blue; acidic residues, red.

show that precise salt bridge architecture (optimized residue pairing, avoidance of intramolecular traps and careful sequence tuning) can stabilize TBPs independently of aromatic stacking.

Simulated structure, membrane affinity and self-assembly of pores

Coarse-grained simulations of de novo-designed peptides revealed pores resembling alamethicin[12] and $(LSSLLSL)_3$ (ref. 1) channels, but with distinct features: larger tilt angles, antiparallel peptide arrangements and engineered salt bridges and stacking interactions (Fig. 3a). These features were validated using 2-µs all-atom simulations (Supplementary Table 10), starting from both initial and final coarse-grained configurations (see Methods). All systems maintained pore integrity with continuous water ion channels (Fig. 3b,c and Supplementary Fig. 3). The ~22-residue amphipathic, transmembrane core remained α-helical, while the termini unfolded outside the membrane. HOLE[36] analysis revealed pore diameters of 10.6–14.2 Å, with constrictions as narrow as 3.6 Å (Fig. 3d,e and Supplementary Fig. 3).

https://doi.org/10.1038/s41589-026-02269-z

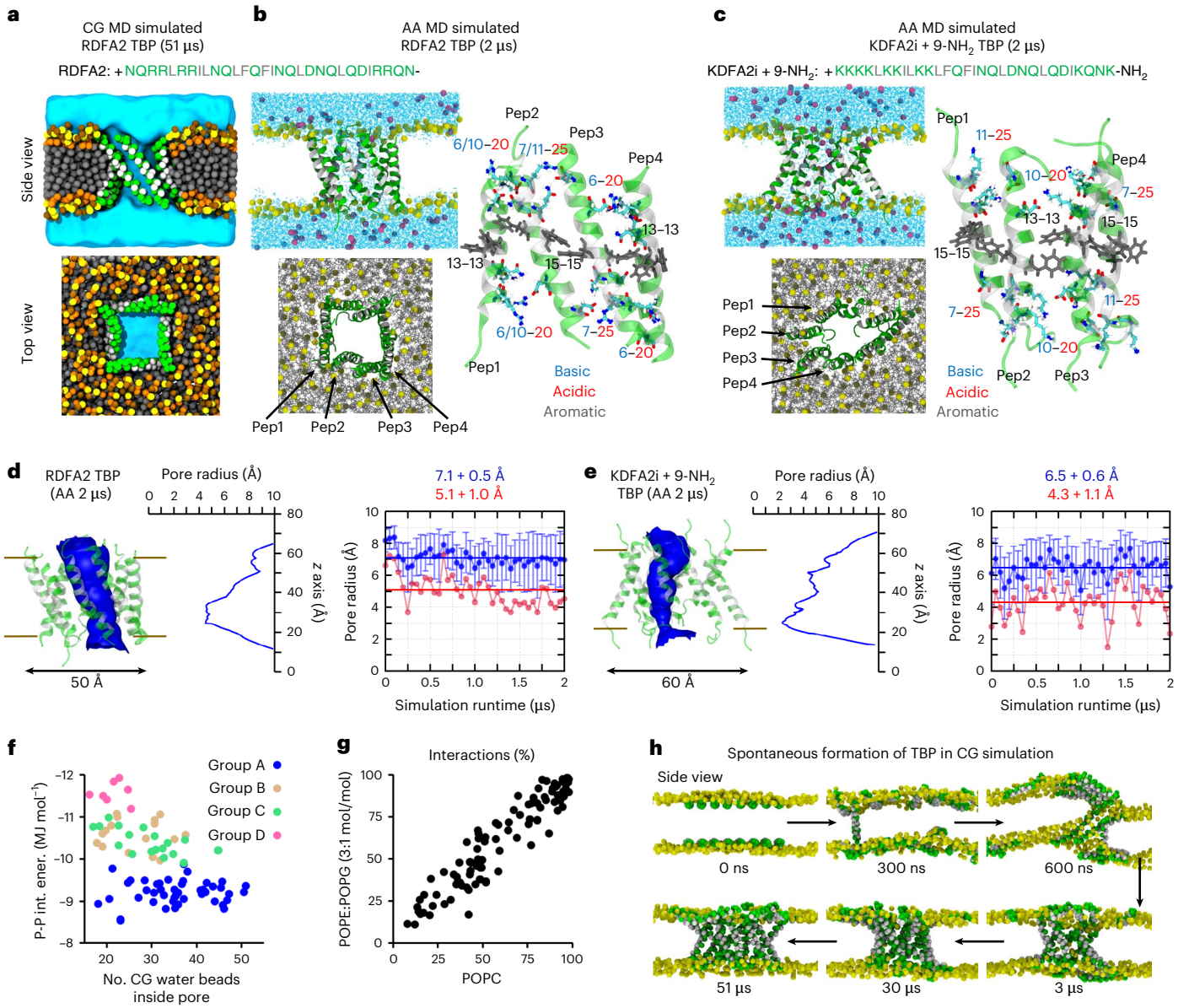

Fig. 3 | TBP structures and their spontaneous assembly. a–c, Snapshots after 51-μs coarse-grained (a) and 2-μs all-atom (b,c) simulations showing octameric TBPs structure with continuous water channel in POPC lipid membrane made by RDFA2 (**a**,**b**) and KDFA2i + 9-NH_2 (**c**) peptides (Supplementary Tables 2 and 10; water, cyan; Na^+, blue; Cl^-, pink). AA, all atom; CG, coarse-grained; Pep, peptide. **d**,**e**, Pore size captured in: left panel, snapshots from all-atom simulations after 2-μs with pore in blue; middle panel, pore radius along the permeation path; and right panel, pore radius (blue) and minimum radius (red) over the 2-μs simulation using POPC lipid membrane and RDFA2 (**d**) and KDFA2i + 9-NH_2 (**e**) peptides. Data represent time-resolved measurements from a single simulation trajectory; mean ± s.d. calculated over trajectory frames. **f**, Correlations between coarse-grained water channels and peptide–peptide interaction energies in TBPs in POPC lipid membrane. P–P int. ener., peptide–peptide interaction energy. **g**, Correlations between interaction strengths in simulations using POPC and POPE:POPG (3:1) lipid membranes. Each point represents the mean designed contact percentage over 51 μs of simulation time, derived from at least three independent simulations for each designed interaction contact. **h**, Coarse-grained snapshots showing spontaneous assembly of a TBP by RDFA2 peptides in POPC:POPG (1:1) lipid membrane (Supplementary Table 11). Color code in snapshots: peptide hydrophilic backbone/residues, green; peptide hydrophobic backbone/residues, white; aromatic residues, silver; basic residues, blue; acidic residues, red; lipid cholines, phosphates, glycerols and tails in ocher, yellow, orange and gray, respectively.

Pore stability increased from group A to D, although stronger interactions narrowed the cavity (Fig. 3f). TBPs remained stable in both zwitterionic POPC and anionic 1-palmitoyl-2-oleoyl-*sn*-glycero-3-phosphoethanolamine:1-palmitoyl-2-oleoyl-*sn*-glycero-3-phospho-1′-rac-glycerol (POPE:POPG; 3:1) bilayers, mimicking eukaryotic and bacterial membranes[37] (Fig. 3g). Cationic peptides exhibited a stronger affinity (~20 kJ mol^{-1}) toward POPE:POPG, owing to stronger interactions with anionic POPG (Supplementary Fig. 4). Spontaneous TBP assembly from surface-adsorbed peptides followed five steps: (1) single-peptide insertion, (2) cooperative insertion with membrane defects, (3) water channel formation, (4) disordered pore assembly and (5) relaxation into a regular TBP (Fig. 3h, Supplementary Fig. 5 and Supplementary Table 11). Larger pores, often exceeding octamers, formed over time. Simulations thus uncovered charge-selective membrane affinity and self-assembly pathways that guided experimental peptide selection.

In vitro pore-forming activity

We synthesized 22 peptides from four design groups (A–D), including arginine/lysine variants with different net charges (pore-stabilizing;

https://doi.org/10.1038/s41589-026-02269-z

Table 1 | In vitro dye leakage and antimicrobial activity

No.	Investigated compounds	Group	Sequences	Solubility in PBS	Dye leakage (%) at P:L 1:100	Antimicrobial activity (MIC)			
						E. coli TOP10		*S. carnosus* CCM4838T	
						μM	μg ml^{-1}	μM	μg ml^{-1}
1	RDWA2	A	NQRRLRRILNQLWQWINQLDNQLQDIRRQN	Aggregated	–	>50	>209	>50	>209
2	RDFA2	A	NQRRLRRILNQLFQFINQLDNQLQDIRRQN	Soluble	80.2	>50	>205	3.1	13
3	KDFA2	A	NQKKLKKILNQLFQFINQLDNQLQDIKKQN	Soluble	82.8	50	197	>50	>197
4	RDFA2i	A	NQRRLRRILNQLFQFINQLDNQLQDIRQNR	Aggregated	–	>50	>205	>50	>205
5	RDFA2i+9-NH_2	A	RRRRLRRILRRLFQFINQLDNQLQDIRQNR-NH_2	Soluble	65.8	1.6	7	0.8	4
6	KDFA2i+9-NH_2	A	KKKKLKKILKKLFQFINQLDNQLQDIKQNK-NH_2	Soluble	87.1	0.8	3	0.8	3
7	RDFA5	A	NQRRLQNILRRLFQFIDQLINDLQNIRRQN	Aggregated	–	>50	>204	>50	>204
8	RDFA7	A	NQRRLQNILRRLFQFINQLIDDLQNIRRQN	Aggregated	–	>50	>202	>50	>202
9	KDFA9	A	NQKKLQNILNKLFKFIDDLINQLQNIKKQN	Soluble	62.6	>50	>195	>50	>195
10	KDFB12	B	KQKKLKKFFNQLIQLINQLFNQLDDFNQNK	Soluble	79.4	6.3	25	6.3	25
11	KD12	B	KQKKLKKILNQLIQLINQLINQLDDINQNK	Soluble	15.7	>50	>192	>50	>192
12	RDFC16	C	NQRRLRRILRRLFQFIDQLDNDLQDIRRQN	Aggregated	–	>50	>212	>50	>212
13	RDFC16K$_{ter}$	C	NQKKLRRILRRLFQFIDQLDNDLQDIKKQN	Soluble	64.5	50	206	>50	>206
14	KDFC16+9-NH_2	C	KKKKLKKILKKLFQFIDQLDNDLQDIKKKK-NH_2	Soluble	78.2	0.8	3	0.4	2
15	KD16+9-NH_2	C	KKKKLKKILKKLIQLIDQLDNDLQDIKKKK-NH_2	Soluble	58.8	6.3	26	3.1	13
16	KDFC16+9SV-NH_2	C	KKKKVKKVVKKVFSFVDSVDSDVSDVKKKK-NH2	Soluble	0.2	25	98	0.4	2
17	DKFC16+9-NH_2	C	KKKKLDDILDDLFQFIKQLKNKLQKIKKKK-NH_2	Soluble	50.1	>50	>208	1.6	7
18	All C16+8	C	KRKRLKRIVKRAWTFMDSVENDLQEIKRKR	Soluble	25.4	25	107	6.3	27
19	RDWC21	C	NQRRLRRILRRLWQWINQLIDDLDDIRRQN	Aggregated	–	>50	>215	>50	>215
20	RDFC21	C	NQRRLRRILRRLFQFINQLIDDLDDIRRQN	Aggregated	–	>50	>211	>50	>211
21	KDFC21+9-NH_2	C	KKKKLKKILKKLFQFINQLIDDLDDIKKKK-NH_2	Soluble	51.9	3.1	13	3.1	13
22	KDFD24+9-NH_2	D	KKKKLKKFFKKLIQLINQLFDDLDDFKKKK-NH_2	Soluble	13.0	12.5	53	12.5	53
23	P28A-NH_2	N	KQNKLQKAANKFAQAFNQADNQLDNAKKQN-NH_2	Soluble	0.5	>50	>183	>50	>183
24	P29-NH_2	N	KQNKLQNFLNQKIQLKNQLFDQLDNIKKQN-NH_2	Soluble	0.3	>50	>197	>50	>197
25	P29A-NH_2	N	KQNKLQNFANQKAQAKNQAFDQADNAKKQN-NH_2	Soluble	0.1	>50	>184	>50	>184
26	P30-NH_2	N	KQNKLQNFLNQFIQKINQKDDQLQNIKKQN-NH_2	Soluble	0.1	>50	>197	>50	>197
27	Alamethicin	R	Ac-UPUAUAQUVUGLUPVUUEQF-ol	Soluble	99.6	–	–	–	–
28	Ampicillin	R	–	Soluble	–	12.5	4	0.1	0.03

Peptide sequences are represented by the one-letter amino acid code U, α-aminoisobutyric acid (U). The N terminus is positively charged or acetylated (Ac-), and the C terminus is negatively charged, amidated (-NH_2) or has a phenylalaninol (-ol) group. Peptides were grouped A–D by the designed interaction density (Supplementary Note 1). Groups N and R indicate negative-control peptides and reference compounds, respectively. All assays were performed in triplicate. Submicromolar antimicrobial activity broadly correlated with leaky pore-forming activity; an MIC of <1 μM was always associated with a reasonable dye leakage, that is, ≥50%, whereas ≥50% leakage did not always yield potent activity (MIC <1 μM). Thus, although pore formation is crucial, factors such as increased membrane affinity via net charge tuning also contribute to enhancing submicromolar potency[8].

Supplementary Note 2); 15 were soluble in PBS (Table 1). Pore formation was evaluated using a standard calcein leakage assay with POPC:POPG (1:1) large unilamellar vesicles (LUVs; Extended Data Fig. 1a), mimicking bacterial membranes[2,29]. Fourteen peptides induced concentration-dependent efflux of the encapsulated fluorescent dye calcein (622.5 Da; Extended Data Fig. 1b). The SV-variant peptide (KDFC16 + 9SV-NH_2) showed no leakage, likely due to narrow, tightly packed pores (see KDFC16 + 8SV, a charged C-terminal variant, in Supplementary Fig. 2d). Eleven peptides caused >50% leakage even at a low peptide-to-lipid (P:L) ratio of 1:100, with the most active exceeding 80% (Table 1). Reduced activity of three peptides was attributed to compromised amphipathicity (All C16 + 9), strong interfacial interactions (KDFD24 + 9-NH_2) or lack of aromatic stacking (KD12). These outcomes support simulation-based predictions that aromatic stacking stabilizes pores in groups A–B, while groups C–D (for example, KD16 + 9-NH_2) form pores independently. Activity was retained in designs with swapped charge-pair positions (DKFC16 + 9-NH_2) and those combining inter- and intramolecular salt bridges (KDFA9). Seven peptides with low net charge (4e$^+$) and clustered arginines were insoluble in PBS but showed sporadic leakage following partial solubilization. Negative-control peptides are described in a separate section below. Notably, KDFA2i + 9-NH_2 emerged as the most potent pore-forming peptide.

In vitro antimicrobial activity

All 22 peptides were tested for antimicrobial activity against Gram-negative *Escherichia coli* TOP10 and Gram-positive *Staphylococcus carnosus* CCM 4838 T (ATCC 51365), BSL-1 strains, using broth microdilution assays (Supplementary Fig. 6a). Antimicrobial activity broadly correlated with dye leakage data (Table 1), supporting pore formation as the likely mechanism. Twelve of the 14 PBS-soluble, pore-forming peptides were active at ≤50 μM, the highest concentration tested. The most potent peptides, KDFC16 + 9-NH_2 and KDFA2i + 9-NH_2, had minimum inhibitory concentrations (MICs) of

0.4–0.8 μM, substantially lower than that of the reference antibiotic ampicillin. Interestingly, KDFC16 + 9SV-NH_2 showed strong activity despite no dye leakage, suggesting pore sizes too narrow for calcein release but sufficient to compromise bacterial viability. Two inactive peptides had low net charge ($4e^+$), lacked aromatic stacking (KD12) or formed intramolecular salt bridges (KDFA9). Overall, increased net charge and arginine-to-lysine substitution improved potency. The most effective AMPs, KDFA2i + 9-NH_2 and KDFC16 + 9-NH_2, were further tested against a panel of ESKAPEE strains (Fig. 4a,b). KDFA2i + 9-NH_2 was more potent, showing MICs of 0.5 μM against *Acinetobacter baumannii* (ATCC 19606) and 1 μM against *E. coli* (AIC221). Both peptides were generally more effective against Gram-negative bacteria, likely due to the thicker peptidoglycan barrier in Gram-positive strains impeding membrane access and pore formation[33].

In vitro toxicity

All 22 peptides were evaluated for hemolytic activity against human red blood cells (HRBCs). Only RDFA2i + 9-NH_2, the arginine variant of KDFA2i + 9-NH_2, was hemolytic (half-maximal inhibitory concentration, (IC_{50}) = 0.9 μM), comparable to the reference hemolytic peptide melittin[2] (Supplementary Fig. 6b). The two lead AMPs, KDFA2i + 9-NH_2 and KDFC16 + 9-NH_2, remained nonhemolytic, with IC_{50} values of 2,594 and 2,691 μM, respectively (Fig. 4c). The arginine-to-lysine substitution markedly reduced cytotoxicity, likely by weakening interactions with zwitterionic membranes[33]. The lead AMPs were also tested against human dermal fibroblasts (HDFs) and embryonic kidney cells (HEK293T), showing IC_{50} values of 10–97 and 6–8 μM, respectively (Fig. 4c). These values translated into broad therapeutic indices (TI = 16–5,200), identifying KDFA2i + 9-NH_2 as a promising lead with high selectivity and a wide therapeutic window.

Bacterial membrane disruption

We tested the two lead AMPs, KDFA2i + 9-NH_2 and KDFC16 + 9-NH_2, for bacterial membrane disruption. In the 3,3′-dipropylthiadicarbocyanine iodide assay[38,39], the peptides depolarized the cytoplasmic membranes of Gram-negative and Gram-positive ESKAPEE pathogens at MIC levels, with effects comparable to or exceeding those of the reference antibiotics polymyxin B and levofloxacin (Fig. 4d and Supplementary Fig. 6c). By contrast, neither peptide permeabilized the outer membrane of Gram-negative pathogens in the 1-(*N*-phenylamino) naphthalene uptake assay[38,39] (Supplementary Fig. 6d), suggesting selective inner membrane targeting. These findings support cytoplasmic membrane depolarization as the dominant antimicrobial mechanism.

Stability in human serum

A key limitation of AMPs is their susceptibility to proteolytic degradation, especially in systemic applications. To assess proteolytic stability, the two lead AMPs, KDFA2i + 9-NH_2 and KDFC16 + 9-NH_2, were incubated in human serum[38,39]. KDFA2i + 9-NH_2 retained ~50% integrity after 6 h, compared to ~15% for KDFC16 + 9-NH_2 (Supplementary Fig. 6e), indicating enhanced serum stability and systemic suitability.

In vivo anti-infective efficacy in animal models

We evaluated the anti-infective efficacy of the lead AMPs KDFA2i + 9-NH_2 and KDFC16 + 9-NH_2 in two preclinical mouse models of *A. baumannii* (ATCC 19606) infection. In a skin abscess model[38,39], the peptides were administered topically at MIC levels (KDFA2i + 9-NH_2: 0.02 mg per kg (body weight); KDFC16 + 9-NH_2: 0.08 mg per kg (body weight)) 1 h after infection (Fig. 4e). Both peptides reduced bacterial burden by one to two orders of magnitude by day 4, whereas the reference antibiotic polymyxin B achieved a 2–3 log reduction. In a deep thigh infection model[38,39], neutropenic mice were treated intraperitoneally at MIC levels (KDFA2i + 9-NH_2: 0.10 mg per kg (body weight); KDFC16 + 9-NH2: 0.41 mg per kg (body weight)) with a single dose 2 h after infection (Fig. 4f). Four days later, KDFA2i + 9-NH_2 reduced bacterial load by 2 logs relative to the vehicle-treated group, whereas KDFC16 + 9-NH_2 was inactive, likely due to its lower serum stability. No weight loss, skin damage or other signs of toxicity were observed (Supplementary Fig. 7a,b). In a scratch infection model of *A. baumannii* (NCTC 13010) infection, topical application of KDFA2i + 9-NH_2 up to 100 mM caused no adverse effects while reducing bacterial burden by ~2 logs within 2 days (Supplementary Fig. 7c). Collectively, these results establish KDFA2i + 9-NH_2 as a lead candidate with potent topical and systemic anti-infective efficacy and a favorable safety profile, supporting its continued development as a therapeutic agent for drug-resistant infections.

Validation of nanopore formation

Having identified KDFA2i + 9-NH_2 as the lead AMP, we next validated the formation of TBPs as its primary antimicrobial mechanism. Circular dichroism spectroscopy confirmed α-helical secondary structure in membrane-mimetic environments[18,19,21,23,25,38,39] (Fig. 5a and Supplementary Fig. 8), consistent with helical TBP assembly. Calcein leakage assays showed detectable leakage (~20%) at an extremely low P:L of 1:2,000, substantial leakage (~45%) at 1:1,000 and marked leakage (~75%) at 1:500 (Fig. 5b), supporting membrane permeabilization via nanopore formation[29,40]. Planar lipid bilayer (PLB) electrophysiology further confirmed stable TBP insertion events, with discrete, stepwise current transitions, which are signatures of barrel-shaped nanopore formation[18,19,21,23,25,41], observed over repeated insertion cycles during a 1-h recording (Fig. 5c and Supplementary Fig. 9). Single-channel conductance scaled linearly with applied voltage, yielding ~0.1-nS and ~0.4-nS conductances at +100 mV in 100 mM and 500 mM NaCl, respectively. Based on cylindrical pore geometry[42] and a bulk conductivity of 1.06 S m^{-1} in 100 mM NaCl[43], we estimated a pore diameter of ~0.8 nm, closely matching the simulated octameric TBP. Real-time atomic force microscopy (AFM) on POPC:POPG (1:1) supported lipid bilayers (SLBs) enabled direct visualization of nanoscale pores within 20 min (imaging start time) at 1 μM (~1:500 P:L), which remained stable over the 3-h imaging period (Fig. 5d and Supplementary Fig. 10). Pores appeared ~6 nm wide (larger than simulated octamers), an approximate value likely influenced by AFM tip convolution and membrane flexibility. At higher concentrations (2–5 μM), similar pores and hexagonal lattice-like assemblies were observed (Supplementary Fig. 11), reminiscent of alamethicin[13]. We noted that these lattice-like membrane features occurred only at high peptide concentrations, where peptide density likely exceeded what can be accommodated within discrete pores, leading to secondary membrane reorganization on supported bilayers. Simulations showed that the designed pores remained stable as large as 16-mers (Supplementary Fig. 12 and Supplementary Table 12). To assess pore size limits of TBPs, we evaluated dextran transport across giant unilamellar vesicles (GUVs). Peptides permitted the entry of 5- and 10-kDa dextrans (~3.4–4.7 nm) but not 60- to 76-kDa dextrans (~11–12 nm; Supplementary Fig. 13), suggesting pore diameters below 11 nm. These estimates are approximate due to dextran deformability and size heterogeneity[44]. Together, these findings provide direct biophysical and nanoscale evidence that KDFA2i + 9-NH_2 forms large, stable and size-tunable TBPs, validating the computationally designed mechanism of antimicrobial action.

Design and validation of negative controls

To validate the importance of residue-specific interactions in stabilizing TBPs, we tested a series of negative-control peptides (P28–P36; Supplementary Table 13), derived from the lead KDFA2i + 9-NH_2. These negative designs retained overall amphipathicity and amino acid composition but were scrambled at positions not expected to support TBP-stabilizing interactions. All designs failed to form stable TBPs in coarse-grained simulations, except P28, which likely stabilized the pore via N-terminal–C-terminal pairing, lipid coordination

https://doi.org/10.1038/s41589-026-02269-z

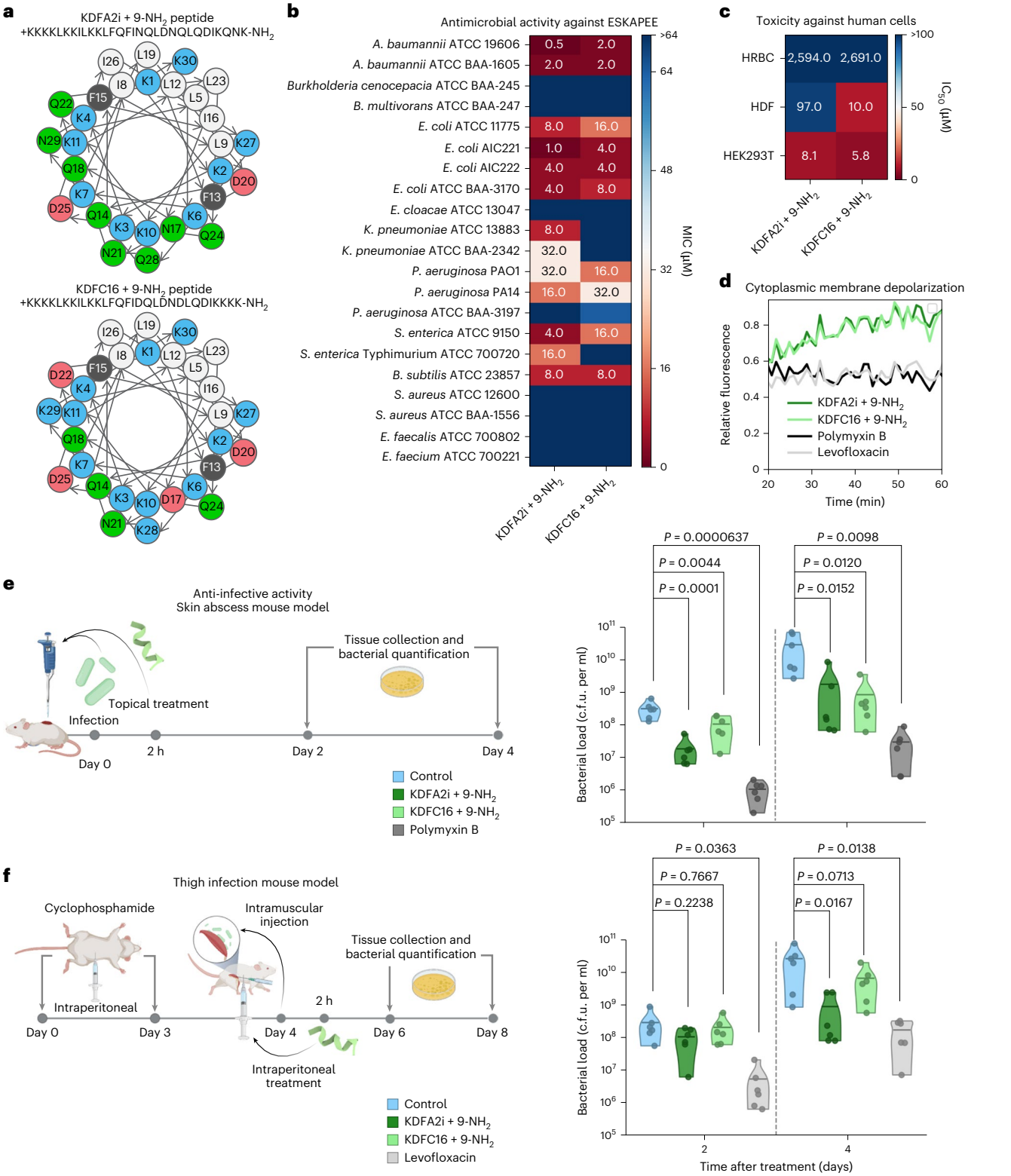

Fig. 4 | In vitro antimicrobial (ESKAPEE) activity and toxicity and in vivo anti-infective efficacy. a, Sequence and helical wheel of lead AMPs KDFA2i + 9-NH_2 and KDFC16 + 9-NH_2. **b**, Submicromolar antimicrobial activity against drug-resistant ESKAPEE pathogens in vitro. **c**, Low cytotoxicity against HRBCs, HDFs and HEK293T cells in vitro. **d**, Depolarization of *A. baumannii* (ATCC 19606) cytoplasmic membrane. Experiments were performed in triplicate. **e**, Schematic of the skin abscess mouse model (*A. baumannii* ATCC 19606). Topical treatment with peptides (MIC-level doses, KDFA2i + 9-NH_2: 0.02 mg perkg (body weight); KDFC16 + 9-NH_2: 0.08 mg per kg (body weight); 2 h after infection) reduced bacterial load by 1–2 logs; the reference antibiotic polymyxin B achieved 2–3 log reduction. **f**, Schematic of the neutropenic thigh infection mouse model (*A. baumannii* ATCC 19606). Intraperitoneal administration of KDFA2i + 9-NH_2 (MIC-level, 0.10 mg per kg (body weight); 2 h after infection) reduced bacterial load by 2 logs, similar to the reference antibiotic levofloxacin; KDFC16 + 9-NH_2 (0.41 mg per kg (body weight)) remained inactive. Experiments were performed with six mice per group. Violin plots show the distributions of individual data points, and horizontal lines indicate means. Statistical significance was determined using a one-way analysis of variance (ANOVA) with a Dunnett's test; *P* values are shown. Illustrations in **e** and **f** created in BioRender; de la Fuente-Nunez, C. https://biorender.com/0yemqjg (2026).

https://doi.org/10.1038/s41589-026-02269-z

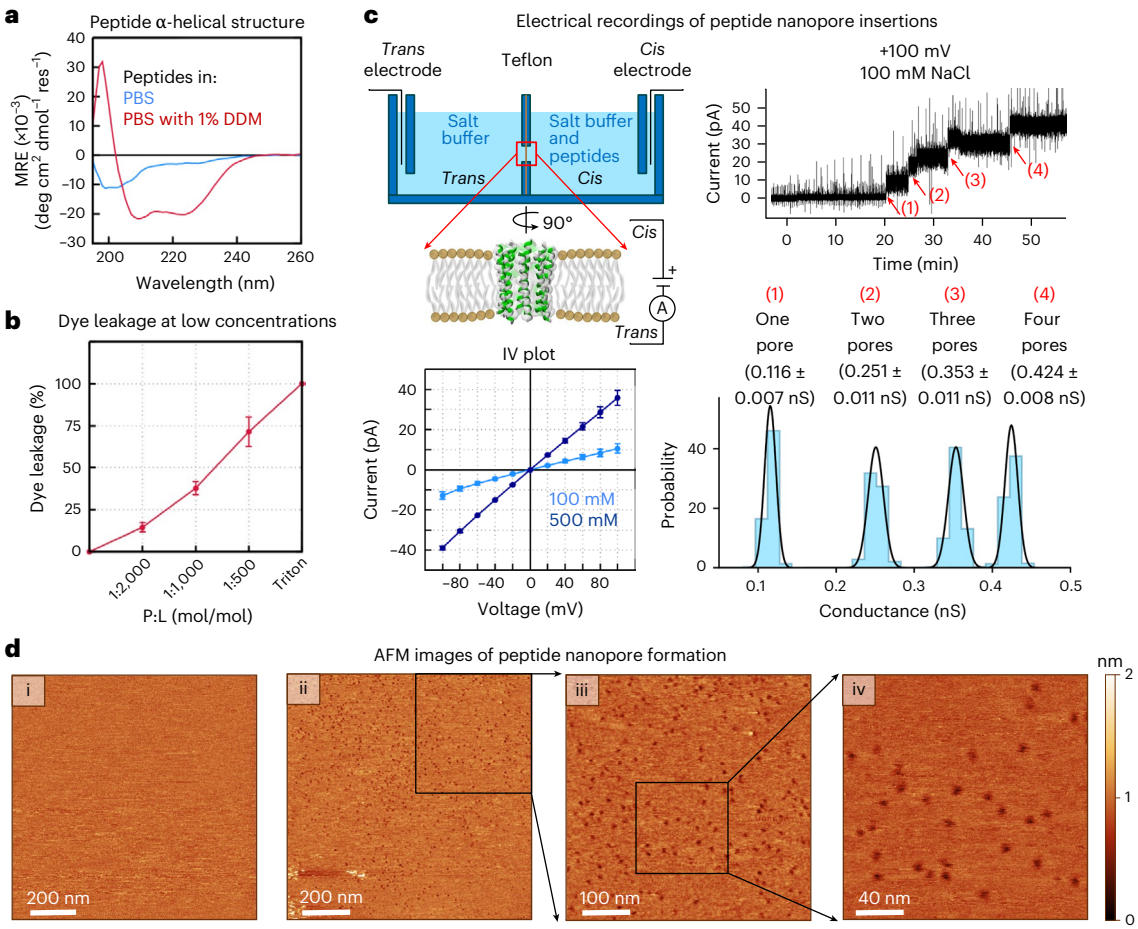

Fig. 5 | Validation of TBP formation by biophysical, electrophysiological and microscopy assays. Evaluation of the lead AMP KDFA2i + 9-NH_2. **a**, Circular dichroism spectra showing the peptide α-helical conformation; assays were performed in triplicate. DDM, *n*-dodecyl-β-d-maltoside; MRE, mean residue ellipticity. **b**, Noticeable calcein release from POPC:POPG (1:1) LUVs at very low peptide concentrations. Triton X-100 caused 100% leakage. Experiments were performed in triplicate. Data are presented as mean ± s.d. **c**, Schematic of the electrophysiological assay (top left); representative stepwise current increases following TBP insertion (peptide concentration: ~500 nM) into a DPhPC PLB, with insertion events marked by red arrows (top right); conductance state distributions for successive pore insertions fitted with Gaussian functions (mean ± s.d. indicated, triplicate experiments; bottom right) and current-voltage (IV) curves for singly inserted TBPs (bottom left). **d**, AFM topographic images of nanopores (peptide concentration: ~1 μM, P:L ratio of 1:500) formed in a POPC:POPG (1:1) SLB. The images show an SLB before peptide addition (i) and SLB after peptide addition with increasing resolution (ii)–(iv). Images from seven additional independent replicates are provided in Supplementary Fig. 10b.

or knobs-into-holes packing[18,22,25]. These effects were abolished after C-terminal amidation and leucine/isoleucine-to-alanine substitutions (P28-NH_2 and P28A-NH_2; Supplementary Table 13). Atomistic simulations confirmed coarse-grained results (Supplementary Table 14). Although simulations assessed TBP stability only (not transient pores or membrane thinning[2]), experiments supported the simulated results: three of four synthesized negative controls showed no calcein leakage, and one caused minimal leakage (≤25%) at a high P:L ratio of 1:10 (Supplementary Fig. 14a). None formed pores in AFM analyses (Supplementary Fig. 14b–e) or showed antibacterial activity (Table 1). These findings confirm the necessity of designed interactions for TBP formation and establish a benchmark for rational nanopore design.

Discussion

This work establishes a systematic framework for the de novo design of transmembrane nanopore-forming peptides by integrating molecular simulations, sequence heuristics and experimental validation, leading to tunable antimicrobial nanopores with demonstrated in vivo efficacy. To efficiently screen sequences, we used a combination of the Martini 2.2 coarse-grained force fields to overcome known limitations[35]. Although Martini does not explicitly resolve fine electronic details such as π–π stacking or subtle arginine–lysine differences, it reliably captures relative interaction trends, which was the primary objective of our large-scale screening. Key predictions were validated by fully atomistic MD simulations, which reproduced the same pore stability trends for designed interaction patterns. Additional simulations elucidated the mechanism of TBP self-assembly, while pore destabilization by the negative-control peptides further validated the importance of the designed interpeptide interactions. Based on the analysis of ~150 designs, we derived residue-level principles to design peptides for TBP formation and formulated design guidelines defining 52 permissible sequence patterns, consolidated into eight templates grouped A–D by the type and number of interpeptide interactions (Methods, Extended Data Fig. 2 and Extended Data Table 1).

Experimental structural determination of transmembrane peptide nanopores at high resolution is challenging due to their small size and dynamic behavior[14,15]. To address this, we combined the use of biophysical assays, electrophysiology, microscopy and transport assays. In liposome leakage assays, the peptides induced efficient release of encapsulated small molecules at low concentrations, indicative of stable pore formation[2,29,40]. To distinguish pore-mediated permeabilization from membrane rupture in the

dextran transport assays, GUV membranes were labeled with the lipid dye 1,1′-dioctadecyl-3,3,3′,3′-tetramethylindodicarbocyanine perchlorate, enabling direct visualization of membrane integrity during peptide exposure (Supplementary Fig. 13). Confocal imaging showed that GUVs remained morphologically intact following dextran entry, supporting pore-mediated permeabilization rather than vesicle rupture. Electrophysiological recordings revealed discrete stepwise conductance events that persisted over time, hallmarks of functional, barrel-shaped nanopores[18,19,21,23,25,41]. Conductance state distributions for successive insertions showed narrow Gaussian profiles with well-separated means (0.116, 0.251, 0.353 and 0.424 nS; Fig. 5c). Direct extraction of step amplitudes yielded $\Delta G = 0.103 \pm 0.021$ nS (mean ± s.d., $n = 4$; Supplementary Fig. 9c), and linear regression demonstrated near-linear scaling of conductance with pore number (slope = 0.103 nS per pore, $R^2 = 0.98$; Supplementary Fig. 9d). Together with proportional scaling with voltage and electrolyte concentration (Fig. 5c), these data support additive single-pore insertion events rather than coincident multipore insertions. AFM imaging directly visualized nanoscale pores that remained stable for hours and revealed larger assemblies (up to ~6 nm), supported by macromolecular transport data, which are in line with simulations of TBP formation at high concentrations, suggesting higher-order polymorphism akin to the natural pore-forming peptide alamethicin[45]. Differences in membrane lipid composition between experimental systems may contribute to variations in apparent pore size and oligomeric state. Simulations revealed enhanced peptide affinity for anionic POPG lipids, consistent with electrostatic recruitment to negatively charged bacterial membranes and likely contributing to antimicrobial selectivity. However, pore formation is not strictly dependent on POPG. In both preformed pore and spontaneous pore formation simulations, stable pores were observed in POPC, POPC:POPG (1:1) and POPE:POPG (3:1) membranes, indicating that the interpeptide interaction network was sufficient to stabilize the barrel-stave architecture once assembled. Experimentally, POPC:POPG (1:1) bilayers were used for solute transport assays and AFM imaging, and peptides were preincubated with POPC:POPG vesicles before electrophysiological measurements. These pore-containing vesicles subsequently fused with zwitterionic 1,2-diphytanoyl-sn-glycero-3-phosphocholine (DPhPC) PLBs for single-channel recordings. The persistence of discrete, stable conductance states after transfer into DPhPC membranes indicates that pore integrity is maintained in the absence of anionic lipids. Together, these findings suggest that anionic lipids facilitate initial membrane recruitment and assembly, whereas pore stability is governed primarily by sequence-encoded interpeptide interactions. Although precise size estimates depend on membrane composition and methodological limitations[44], the concordance between simulations and experiments substantiates the formation of stable, functional transmembrane nanopores.

The designed cationic peptides exhibited potent antimicrobial activity against drug-resistant ESKAPEE pathogens, with minimal cytotoxicity toward human cells. Peptide activity and selectivity were rationally tuned by modifying the termini and hydrophilic face; adding cationic residues increased affinity for negatively charged bacterial membranes without affecting zwitterionic human membranes[5,6,33]. These modifications enhanced antibacterial potency without compromising pore-forming ability or safety. Mechanistically, the peptides depolarized bacterial inner membranes, similar to known AMPs. KDFA2i + 9-NH_2 emerged as the most potent pore-forming AMP. Its antimicrobial activity appears to result from nanopore-mediated membrane disruption, as supported by both simulations and experiments. KDFA2i + 9-NH_2 exhibited submicromolar efficacy against *A. baumannii*, a World Health Organization priority pathogen[10], along with high serum stability and no observable toxicity, making it a promising lead for systemic and topical treatment of drug-resistant infections. In two preclinical mouse models of *A. baumannii* infection (skin abscess (topical) and deep thigh infection (intraperitoneal)[38,39]), the peptide demonstrated anti-infective efficacy, validating its translational potential. Resistance evolution experiments with *A. baumannii* (ATCC 19606) under stepwise exposure to KDFA2i + 9-NH_2 produced only a transient increase in MIC. This increase was reversible, stabilizing at a level one dilution above the starting MIC after the removal of selective pressure (Supplementary Fig. 15), indicating reversible adaptation rather than stable genetic resistance.

Benchmarking KDFA2i + 9-NH_2 against the natural barrel-stave pore former alamethicin provides a reference for assessing whether the designed nanopores reproduce canonical pore behavior while enabling tunable structural features. KDFA2i + 9-NH_2 closely matches alamethicin in its electrophysiological signatures, exhibiting discrete stepwise current insertions, stable open states and single-channel conductances in the same range under comparable ionic conditions[46–48], consistent with ohmic transport through water-filled pores. Circular dichroism measurements further showed that the designed peptides adopted predominantly α-helical conformations, similar to alamethicin. However, the terminal eight residues were intentionally designed to be polar for functional tuning; accordingly, only minor terminal fraying was expected and was supported by all-atom simulations, which revealed stable helical cores with limited flexibility at the termini. Both peptides also showed efficient calcein leakage from LUVs at similar P:L ratios (Table 1), indicating comparable pore-forming efficacy for small solutes. By contrast, alamethicin did not permit 4-kDa dextran permeation at P:L ratios up to 1:37.5 to 1:50 and instead caused vesicle rupture at higher peptide loading (P:L = 1:25), while still allowing calcein permeation in GUVs under the same conditions (Supplementary Fig. 13c,d), consistent with its reported pore diameter of ~1.5–1.8 nm and size-limited transport[49–51]. However, KDFA2i + 9-NH_2 permitted 4-kDa dextran transport already at a P:L ratio of 1:50, indicating the formation of wider and more permissive nanopores. Notably, whereas alamethicin assembles in parallel orientations, our designed peptides preferentially form stable pores with antiparallel arrangements, which are encoded by complementary distributions of hydrophobic, aromatic and charged residues that stabilize interpeptide packing within the barrel-stave architecture. Consistent with this design logic, simulations initiated from parallel peptide arrangements rapidly destabilized the pore (Supplementary Fig. 16), whereas antiparallel assemblies relaxed into long-lived pore structures (Supplementary Fig. 12), and peptides initially adsorbed in parallel orientations reorganized into antiparallel configurations during spontaneous pore formation (Supplementary Fig. 5). These results show that antiparallel organization is energetically preferred and arises from the designed interpeptide interaction network. Although the peptides were designed to form octameric pores, alternative oligomeric states were accessible: simulations spanning 8–16 subunits showed consistent stability trends (Supplementary Fig. 12), and spontaneous assembly frequently produced larger antiparallel pores exceeding 8-mers (Supplementary Fig. 5). Peptide tilt likewise converged to values dictated by hydrophobic mismatch rather than initial placement: sequences with a 22-residue hydrophobic segment adopted an ~30° tilt even when initialized nontilted, whereas extended hydrophobic cores exhibited larger tilts (~50°) and failed to stabilize pores without the engineered interaction network. Overall, pore architecture, oligomer size, orientation and tilt emerge from the designed sequence-encoded interactions rather than from the starting structural configuration.

To assess how predictive the computational design metrics are for experimental function beyond the lead peptide, we examined the correlation between MD simulations and experimental results using the 15 peptides soluble in PBS (Table 1). Peptide–peptide interaction energy and pore hydration (that is, the number of water molecules inside the pore) obtained from simulations were compared

to experimental readouts (dye leakage and antimicrobial activity; Supplementary Fig. 17). With a few exceptions, the simulation outcomes showed good agreement with the dye leakage data: dye leakage increased with increasing simulated pore hydration and decreasing peptide–peptide interaction energy. This trend reflects changes in packing geometry across design groups (A–D), where narrower pore cavities exhibit reduced pore hydration and correspondingly lower dye leakage. By contrast, no clear correlation was observed between simulated pore hydration or peptide–peptide interaction energy and in vitro antimicrobial activity (against *E. coli* and *S. carnosus*). These results indicate that pore-forming ability alone is not sufficient for bacterial killing, consistent with our previous findings that additional factors, such as peptide affinity for bacterial membranes, are critical for achieving submicromolar to nanomolar antimicrobial activity[8]. Accordingly, although the present study establishes generalizable design principles for TBPs, further optimization will be required to tailor these peptides for specific applications, including antimicrobial therapeutics and biotechnology. Such optimization may, for example, involve sequence refinement to balance activity, selectivity and stability in application-specific contexts.

To evaluate whether recent structure-prediction methods could inform the assembly of transmembrane peptide nanopores, we explored the use of AlphaFold-based approaches. Peptide oligomerization (8-mers) was modeled using AlphaFold2-Multimer (v3) via ColabFold[52], testing multiple parameter sets, including variations in multiple sequence alignment depth, recycles, seeds and iterations. In all cases, AlphaFold2-Multimer yielded α-helical monomers and aggregated assemblies but did not produce barrel-stave pore architectures (Supplementary Fig. 18a), which is likely due to the absence of an explicit lipid environment. Next, using AlphaFold 3, we linked eight peptides with GGGGS spacers in the absence and presence of lipid ligands (oleic acid or palmitic acid)[53]. Without ligands, AlphaFold 3 predominantly generated dimer-of-tetramer assemblies (Supplementary Fig. 18b). In the presence of lipid ligands, the models resembled lipid nanodisc-like structures, in which lipids formed a bilayer-like core surrounded by α-helical peptides; increasing ligand numbers expanded these assemblies and weakened peptide–peptide interfaces (Supplementary Fig. 18c). In none of these cases did AlphaFold yield a membrane-inserted barrel-stave pore, highlighting the current limitations of AlphaFold-based methods for predicting transmembrane peptide nanopore assembly and underscoring the importance of membrane-explicit simulation approaches.

By combining large-scale molecular simulations with multiscale validation and targeted experiments, this study provides a systematic and experimentally validated computational pipeline for the de novo design of transmembrane peptide nanopores with preclinically validated antimicrobial activity. The principal advance lies in establishing general design principles that link peptide sequence to pore architecture, stability, transport properties and biological activity, enabling these features to be rationally tuned rather than discovered empirically in the development of peptide-based therapeutics. Through sequence-level tunability, these peptides could be adapted into next-generation anticancer agents that selectively disrupt malignant cell membranes[8]. Their modularity, programmability and synthetic accessibility position them for applications in nanobiotechnology, including as biosensors and in responsive delivery systems[3,4]. These insights pave the way for broader deployment of synthetic nanopores in therapeutic and diagnostic applications.

Online content

Any methods, additional references, Nature Portfolio reporting summaries, source data, extended data, supplementary information, acknowledgements, peer review information, details of author contributions and competing interests, and statements of data and code availability are available at https://doi.org/10.1038/s41589-026-02269-z.

References

1. Lear, J. D., Wasserman, Z. R. & DeGrado, W. F. Synthetic amphiphilic peptide models for protein ion channels. *Science* **240**, 1177–1181 (1988).
2. Guha, S., Ghimire, J., Wu, E. & Wimley, W. C. Mechanistic landscape of membrane-permeabilizing peptides. *Chem. Rev.* **119**, 6040–6085 (2019).
3. Majd, S. et al. Applications of biological pores in nanomedicine, sensing, and nanoelectronics. *Curr. Opin. Biotechnol.* **21**, 439–476 (2010).
4. Howorka, S. Building membrane nanopores. *Nat. Nanotechnol.* **12**, 619–630 (2017).
5. Zasloff, M. Antimicrobial peptides of multicellular organisms. *Nature* **415**, 389–395 (2002).
6. Yeaman, M. R. & Yount, N. Y. Mechanisms of antimicrobial peptide action and resistance. *Pharmacol. Rev.* **55**, 27–55 (2003).
7. Brogden, K. A. Antimicrobial peptides: pore formers or metabolic inhibitors in bacteria? *Nat. Rev. Microbiol.* **3**, 238–250 (2005).
8. Deb, R. et al. Computational design of pore-forming peptides with potent antimicrobial and anticancer activities. *J. Med. Chem.* **67**, 14040–14061 (2024).
9. Lazzaro, B. P., Zasloff, M. & Rolff, J. Antimicrobial peptides: application informed by evolution. *Science* **368**, eaau5480 (2020).
10. Magana, M. et al. The value of antimicrobial peptides in the age of resistance. *Lancet Infect. Dis.* **20**, e216–e230 (2020).
11. Wang, G., Li, X. & Wang, Z. APD3: the antimicrobial peptide database as a tool for research and education. *Nucleic Acids Res.* **44**, D1087–D1093 (2016).
12. Fox, R. O. Jr & Richards, F. M. A voltage-gated ion channel model inferred from the crystal structure of alamethicin at 1.5-Å resolution. *Nature* **300**, 325–330 (1982).
13. Pieta, P., Mirza, J. & Lipkowski, J. Direct visualization of the alamethicin pore formed in a planar phospholipid matrix. *Proc. Natl Acad. Sci. USA* **109**, 21223–21227 (2012).
14. Korendovych, I. V. & DeGrado, W. F. De novo protein design, a retrospective. *Q. Rev. Biophys.* **53**, e3 (2020).
15. Woolfson, D. N. A brief history of de novo protein design: minimal, rational, and computational. *J. Mol. Biol.* **433**, 167160 (2021).
16. Tuerkova, A. et al. Effect of helical kink in antimicrobial peptides on membrane pore formation. *eLife* **9**, e47946 (2020).
17. Joh, N. H. et al. De novo design of a transmembrane Zn^{2+}-transporting four-helix bundle. *Science* **346**, 1520–1524 (2014).
18. Scott, A. J. et al. Constructing ion channels from water-soluble α-helical barrels. *Nat. Chem.* **13**, 643–650 (2021).
19. Mahendran, K. R. et al. A monodisperse transmembrane α-helical peptide barrel. *Nat. Chem.* **9**, 411–419 (2017).
20. Lu, P. et al. Accurate computational design of multipass transmembrane proteins. *Science* **359**, 1042–1046 (2018).
21. Krishnan, R. S. et al. Autonomously assembled synthetic transmembrane peptide pore. *J. Am. Chem. Soc.* **141**, 2949–2959 (2019).
22. Mravic, M. et al. Packing of apolar side chains enables accurate design of highly stable membrane proteins. *Science* **363**, 1418–1423 (2019).
23. Krishnan, R. S. et al. Assembly of transmembrane pores from mirror-image peptides. *Nat. Commun.* **13**, 5377 (2022).
24. Xu, C. et al. Computational design of transmembrane pores. *Nature* **585**, 129–134 (2020).
25. Niitsu, A. et al. Rational design principles for de novo α-helical peptide barrels with dynamic conductive channels. *J. Am. Chem. Soc.* **147**, 11741–11753 (2025).
26. Wang, Y., Chen, C. H., Hu, D., Ulmschneider, M. B. & Ulmschneider, J. P. Spontaneous formation of structurally diverse membrane channel architectures from a single antimicrobial peptide. *Nat. Commun.* **7**, 13535 (2016).

27. de Jong, D. H. et al. Improved parameters for the Martini coarse-grained protein force field. *J. Chem. Theory Comput.* **9**, 687–697 (2013).
28. Bowie, J. U. Helix packing in membrane proteins. *J. Mol. Biol.* **272**, 780–789 (1997).
29. Chen, C. H. et al. Simulation-guided rational de novo design of a small pore-forming antimicrobial peptide. *J. Am. Chem. Soc.* **141**, 4839–4848 (2019).
30. Ridder, A., Skupjen, P., Unterreitmeier, S. & Langosch, D. Tryptophan supports interaction of transmembrane helices. *J. Mol. Biol.* **354**, 894–902 (2005).
31. Unterreitmeier, S. et al. Phenylalanine promotes interaction of transmembrane domains via GxxxG motifs. *J. Mol. Biol.* **374**, 705–718 (2007).
32. Walther, T. H. & Ulrich, A. S. Transmembrane helix assembly and the role of salt bridges. *Curr. Opin. Struct. Biol.* **27**, 63–68 (2014).
33. Bobone, S. & Stella, L. in *Antimicrobial Peptides: Basics for Clinical Application* (ed. Matsuzaki, K.) 175–214 (Springer, 2019).
34. Dawson, J. P., Weinger, J. S. & Engelman, D. M. Motifs of serine and threonine can drive association of transmembrane helices. *J. Mol. Biol.* **316**, 799–805 (2002).
35. Javanainen, M., Martinez-Seara, H. & Vattulainen, I. Excessive aggregation of membrane proteins in the Martini model. *PLoS ONE* **12**, e0187936 (2017).
36. Smart, O. S., Neduvelil, J. G., Wang, X., Wallace, B. A. & Sansom, M. S. P. HOLE: a program for the analysis of the pore dimensions of ion channel structural models. *J. Mol. Graph.* **14**, 354–360 (1996).
37. Mani, R. et al. Membrane-dependent oligomeric structure and pore formation of a β-hairpin antimicrobial peptide in lipid bilayers from solid-state NMR. *Proc. Natl Acad. Sci. USA* **103**, 16242–16247 (2006).
38. Torres, M. D. T. et al. Mining for encrypted peptide antibiotics in the human proteome. *Nat. Biomed. Eng.* **6**, 67–75 (2022).
39. Wan, F., Torres, M. D. T., Peng, J. & de la Fuente-Nunez, C. Deep-learning-enabled antibiotic discovery through molecular de-extinction. *Nat. Biomed. Eng.* **8**, 854–871 (2024).
40. Krauson, A. J., He, J. & Wimley, W. C. Gain-of-function analogues of the pore-forming peptide melittin selected by orthogonal high-throughput screening. *J. Am. Chem. Soc.* **134**, 12732–12741 (2012).
41. Shimizu, K. et al. De novo design of a nanopore for single-molecule detection that incorporates a β-hairpin peptide. *Nat. Nanotechnol.* **17**, 67–75 (2022).
42. Soskine, M., Biesemans, A., De Maeyer, M. & Maglia, G. Tuning the size and properties of ClyA nanopores assisted by directed evolution. *J. Am. Chem. Soc.* **135**, 13456–13463 (2013).
43. McCleskey, R. B. Electrical conductivity of electrolytes found in natural waters from (5 to 90) °C. *J. Chem. Eng. Data* **56**, 317–327 (2011).
44. Bertrand, B., Garduño-Juárez, R. & Munoz-Garay, C. Estimation of pore dimensions in lipid membranes induced by peptides and other biomolecules: a review. *Biochim. Biophys. Acta Biomembr.* **1863**, 183551 (2021).
45. Harriss, L. M., Cronin, B., Thompson, J. R. & Wallace, M. I. Imaging multiple conductance states in an alamethicin pore. *J. Am. Chem. Soc.* **133**, 14507–14509 (2011).
46. Eisenberg, M., Hall, J. E. & Mead, C. A. The nature of the voltage-dependent conductance induced by alamethicin in black lipid membranes. *J. Membr. Biol.* **14**, 143–176 (1973).
47. Sakmann, B. & Boheim, G. Alamethicin-induced single channel conductance fluctuations in biological membranes. *Nature* **282**, 336–339 (1979).
48. Okazaki, T., Sakoh, M., Nagaoka, Y. & Asami, K. Ion channels of alamethicin dimer N-terminally linked by disulfide bond. *Biophys. J.* **85**, 267–273 (2003).
49. Sansom, M. S. The biophysics of peptide models of ion channels. *Prog. Biophys. Mol. Biol.* **55**, 139–235 (1991).
50. Woolley, G. A. & Wallace, B. A. Model ion channels: gramicidin and alamethicin. *J. Membr. Biol.* **129**, 109–136 (1992).
51. Qian, S., Wang, W., Yang, L. & Huang, H. W. Structure of the alamethicin pore reconstructed by X-ray diffraction analysis. *Biophys. J.* **94**, 3512–3522 (2008).
52. Mirdita, M. et al. ColabFold: making protein folding accessible to all. *Nat. Methods* **19**, 679–682 (2022).
53. Abramson, J. et al. Accurate structure prediction of biomolecular interactions with AlphaFold 3. *Nature* **630**, 493–500 (2024).

[1]Central European Institute of Technology (CEITEC), Masaryk University, Brno, Czech Republic. [2]National Centre for Biomolecular Research, Faculty of Science, Masaryk University, Brno, Czech Republic. [3]Department of Pharmaceutical Technology, JIS University, Kolkata, India. [4]Machine Biology Group, Departments of Psychiatry and Microbiology, Institute for Biomedical Informatics, Institute for Translational Medicine and Therapeutics, Perelman School of Medicine, University of Pennsylvania, Philadelphia, PA, USA. [5]Departments of Bioengineering, School of Engineering and Applied Science, University of Pennsylvania, Philadelphia, PA, USA. [6]Penn Institute for Computational Science, University of Pennsylvania, Philadelphia, PA, USA. [7]Department of Chemistry, School of Arts and Sciences, University of Pennsylvania, Philadelphia, PA, USA. [8]Department of Chemical and Biomolecular Engineering, School of Engineering and Applied Science, University of Pennsylvania, Philadelphia, PA, USA. [9]Institute of Molecular and Translational Medicine, Faculty of Medicine and Dentistry, Palacký University, Olomouc, Czech Republic. [10]Groningen Biomolecular Science and Biotechnology Institute, University of Groningen, Groningen, the Netherlands. [11]Institute of Microbiology, Czech Academy of Sciences, BIOCEV, Vestec, Czech Republic. [12]Institute of Molecular and Translational Medicine, University Hospital, Olomouc, Czech Republic. [13]Czech Advanced Technology and Research Institute, Palacký University, Olomouc, Czech Republic. [14]Department of Condensed Matter Physics, Faculty of Science, Masaryk University, Brno, Czech Republic.
✉e-mail: robert.vacha@muni.cz

Methods

A concise description of the methodology used in this study is provided here. The Supplementary Information contains a more detailed description of both the methods and materials used.

Computer simulations

Coarse-grained MD simulations were performed using GROMACS 5.1.4 (ref. 54) and the Martini 2.2 force field[27,55], unless stated otherwise. Helical all-atom peptide structures were converted to coarse-grained representations via martinize.py[27], retaining charged termini (N^+, C^-); C-terminal amidation was modeled by removing the $1e^-$ charge and modifying the backbone bead type as recommended[27]. Lipid bilayers were constructed using CHARMM-GUI Martini Maker[56] with three compositions: POPC, POPC:POPG (1:1) and POPE:POPG (3:1). Systems were solvated with ~12,000 standard Martini water beads and neutralized with 0.154 M NaCl.

The following three simulation types were performed. (1) Preformed membrane pore simulations. To evaluate pore stabilization, peptides were placed around a preformed 2-nm pore in bilayers with a P:L ratio of 8:504. Peptides were oriented antiparallel and perpendicular to the membrane. After equilibration with the pore constraint, 51-µs unbiased simulations were run. Pores were classified as stable (eight transmembrane peptides, continuous water), deformed (four to seven transmembrane peptides) or closed (less than four transmembrane peptides, no water). Selected systems were simulated unbiased for another 51 µs with a 10%-scaled Martini force field[35]. Additional oligomeric states (4–16 peptides) were simulated with adjusted pore radii. (2) Umbrella sampling simulations. The potential of mean force of peptide adsorption on bilayers was calculated along the membrane normal (*z* axis) between the membrane and peptide centers of mass via the umbrella sampling method[57]. One peptide was placed on each leaflet of a 240-lipid bilayer and pulled 4 nm along the membrane normal (*z* axis). Umbrella windows were spaced at 0.1 nm and simulated for 550 ns. (3) Self-assembly simulations: Peptide self-assembly into transmembrane barrel pores was simulated at P:L ratios of 16:504, 24:504 and 32:504. Peptides were symmetrically placed on each leaflet with hydrophobic sides facing inward at the following three depths: (1) in solution, (2) head–water interface and (3) head–tail interface. Simulations were run for 30 µs and extended to 51 µs if pores formed. Otherwise, an inverted flat-bottom potential was applied to aid transmembrane insertion.

Systems were energy minimized with steepest descent algorithm and equilibrated in five constant number of particles, pressure and temperature (NPT) steps (~1 µs). Production runs used a 30-fs time step with the leap-frog integrator. Temperature (320 K) was maintained using a velocity-rescale thermostat[58] ($\tau = 1$ ps). Pressure (1 bar) was controlled semi-isotropically using the Parrinello–Rahman barostat[59] ($\tau = 12$ ps, compressibility = 3×10^{-4} bar^{-1}). Periodic boundary conditions and the Verlet cutoff scheme[60] (1.1-nm cutoff, 20-step neighbor list update) were used. The van der Waals and Coulomb interactions were cutoff at 1.1 nm; Coulomb interactions were treated via reaction-field[61] (relative dielectric constant of 15). Bonds were constrained using LINCS[62].

Coarse-grained systems were back-mapped to all-atom resolution using *initram.sh*[63], with the AMBERff99SB-ILDN[64] and SLIPIDS[65] force fields and TIP3P water[66]. Two all-atom simulation sets were run: one from coarse-grained-equilibrated systems and another from final coarse-grained snapshots using GROMACS 2021.4. Energy-minimized all-atom systems were shortly equilibrated in the constant number of particles, volume and temperature ensemble (NVT), then equilibrated in NPT for 50 ns and finally simulated for 2 µs using 2-fs time steps. A Verlet cutoff scheme[60] with a 1.2-nm cutoff and ten-step neighbor list update were used for nonbonded interactions, with the particle-mesh Ewald method[67] for electrostatics (1.2-nm cutoff) and the force-switch function[68] (between 1.0 and 1.2 nm) for van der Waals interactions. Temperature (303 K) and pressure (1 bar) were maintained with a velocity-rescale thermostat[58] ($\tau = 1$ ps) and semi-isotropic Parrinello–Rahman barostat[59] ($\tau = 2$ ps, compressibility = 4.5×10^{-5} bar^{-1}).

Simulations were visually analyzed using visual MD[69]. Water occupancy within pores was computed in a 2-nm slab around the membrane center. Peptide tilt was defined as the angle between the helical axis and the membrane normal (*z* axis). Pore radius and permeation paths were determined using HOLE[36]. The π–π stacking and salt bridges were defined within a cutoff distance of 0.8 nm, based on radial distribution functions (Supplementary Fig. 19). Interaction stability was assigned if present ≥50% of the simulation time. Umbrella sampling data were analyzed using the WHAM method[70].

Peptide synthesis

Peptides were synthesized with >95% purity (using HPLC) by JPT Peptide Technologies, Apigenex and Caslo.

Antimicrobial assays

Antimicrobial activity was evaluated against *E. coli* (TOP10) and *S. carnosus* (CCM 4838 T) using the broth microdilution method. PBS buffer was prepared as follows: 1.8 mM $NaH_2PO_4{\cdot}H_2O$, 10 mM $Na_2HPO_4{\cdot}7H_2O$, 135 mM NaCl and 4.5 mM KCl; Mueller–Hinton broth and Mueller–Hinton agar solutions contained 5.25 g and 9.50 g of these powders, respectively, in 250 ml of water. Mid-log-phase cultures (10^6 colony forming unit (c.f.u.) per ml) were exposed to peptides (0.1–50 µM) in Mueller–Hinton broth in 96-well plates and incubated at 37 °C for 24 h. MIC was defined as the lowest concentration preventing visible growth of bacteria. Bactericidal or bacteriostatic effects were assessed by subculturing from MIC wells onto agar plates. For ESKAPEE strains (*A. baumannii* (ATCC 19606 and BAA-1605), *E. coli* (ATCC 11775, AIC221, AIC222 and BAA-3170), *E. cloacae* (ATCC 13047), *Klebsiella pneumoniae* (ATCC 13883 and BAA-2342), *Pseudomonas aeruginosa* (PAO1, PA14 and ATCC BAA-3197), *Salmonella enterica* (ATCC 9150 and Typhimurium ATCC 700720), *Bacillus subtilis* (ATCC 23857), *Burkholderia cenopecacia* (ATCC BAA-245), *Burkholderia multivorans* (ATCC BAA-247), *Staphylococcus aureus* (ATCC 12600 and BAA-1556), *Enterococcus faecalis* (ATCC 700802) and *E. faecium* (ATCC 700221)), similar assays were performed in LB medium with ~4×10^6 cells per ml, followed by a 24-h incubation and visual MIC determination. All measurements were performed in triplicate.

Cytotoxicity assays

Peptide-induced hemolysis was assessed using HRBCs (type A^-, male donor; Zen-Bio). For screening, erythrocytes were washed, resuspended in PBS (0.5% vol/vol) and incubated with peptides (0.1–50 µM) in 96-well plates at 37 °C for 1 h. Melittin (5 µM) and PBS served as the positive (100%) and negative (0%) lysis controls, respectively. After centrifugation, hemoglobin release in supernatants was quantified by absorbance at 415 nm using a Tecan Infinite F500 plate reader. For selected lead peptides, IC_{50} values were determined from normalized data using an extended concentration range.

To assess toxicity against HDFs, cytotoxicity assays were performed as a service by Essence Line at Sterlab using a neutral red uptake assay. Cells were seeded at 1×10^4 cells per well in 96-well plates and incubated for 24 h in DMEM at 37 °C. Peptides (0.5–150 µM) were added in fresh medium, and cells were incubated for an additional 24 h. SDS (0.5%) and untreated wells served as positive and negative controls, respectively. After PBS washing, cells were incubated with neutral red (50 µg ml^{-1}) for 3 h, followed by destaining (ethanol:acetic acid:water, 50:1:49 vol/vol/vol). Absorbance was recorded at 540 nm, and IC_{50} values were calculated from normalized absorbance values.

To assess toxicity against HEK293T cells, cells were seeded in 96-well plates (5,000 cells per well) and treated with peptides (8–128 µM) for 24 h. Cell viability was assessed using an MTT assay. After incubation with MTT reagent (0.5 mg ml^{-1}) in phenol red-free medium for 4 h at 37 °C, formazan crystals were solubilized in 0.04 M

HCl in isopropanol. Absorbance was measured at 570 nm. All assays were performed in triplicate.

Cytoplasmic membrane depolarization assay

Bacteria (optical density at 600 nm (OD_{600}) = 0.5) were washed twice with buffer (20 mM glucose, 5 mM HEPES, pH 7.2), and diluted 1:10 in depolarization buffer (0.1 M KCl, 20 mM glucose, 5 mM HEPES, pH 7.2). After incubating 100 µl of the bacterial suspension with 20 nM 3,3′-dipropylthiadicarbocyanine iodide for 15 min, peptides (100 µl at MICs) were added[38,39]. Fluorescence was recorded at λ_{ex} = 622 nm and λ_{em} = 670 nm. All experiments were performed in triplicate.

Outer membrane permeabilization assay

Bacteria (OD_{600} = 0.4) were washed and resuspended in a buffer containing 5 mM HEPES and 5 mM glucose (pH 7.4). Four microliters of 1-(*N*-phenylamino) naphthalene solution (10 mM) was added to 100 µl of the bacterial suspension in 96-well plates. Peptides (100 µl at MICs) were added, and fluorescence (λ_{ex} = 350 nm, λ_{em} = 420 nm) was recorded for 45 min (refs.38,39). Assays were performed in triplicate.

Peptide stability in human serum assay

Peptides (10 mg ml^{-1}) were incubated in 25% human serum (in water) at 37 °C (refs. 38,39). Aliquots (100 µl) were collected at 0, 0.5, 1, 3 and 6 h and treated with 10 µl TFA (100%) to precipitate serum proteins, followed by a 10-min incubation on ice. Samples were analyzed using UPLC–MS (Waters ACQUITY HSS C18, 1.8 µm, 2.1 × 50 mm; ESI±, *m*/*z* 100–2,000) with photodiode array detection. The mobile phases were water or acetonitrile (both with 0.1% formic acid). Peptide stability was determined by area under the curve integration of the parent ion relative to time zero. Data represent three independent replicates.

Skin abscess infection mouse model

A. baumannii (ATCC 19606; OD_{600} = 0.5) was washed and resuspended in PBS (1×10^6 c.f.u. per ml), and 20 µl of this suspension was applied to needle-abraded skin of anesthetized, shaved female CD-1 mice (6 weeks old; Charles River Laboratories)[38,39]. After 2 h, peptides (at MICs) or sterile water (control) were applied to the skin. Infected skin was excised on days 2 and 4 after infection, homogenized (25 Hz, 20 min) and serially diluted for c.f.u. quantification on MacConkey agar. Experiments were blinded with six mice per group, and no animals were excluded. Data were analyzed using a one-way ANOVA with a Dunnett's test on $\log_{10}$-transformed c.f.u. values to minimize outlier effects using GraphPad Prism (v10.4.2).

Scratch infection mouse model

Immunosuppressed female BALB/c mice (8–10 weeks old; Anlab/Inotiv) received two intraperitoneal injections of cyclophosphamide (150 and 100 mg per kg (body weight)) on days −5 and −1 before wounding. Mice received two 12-mm dorsal scratches inoculated with 20 µl of *A. baumannii* NCTC 13010 (3×10^6 c.f.u.). Treatment started 2 h after infection: group 1: 10 mM peptide; group 2: 100 mM peptide; group 3: 10 mM colistin; group 4: 100 mM colistin (n = 4 per group). Each scratch received 20 µl of solution and was allowed to dry. On day 2, wounds were excised by deep abrasion, homogenized in 1 ml of PBS, serially diluted and plated on MacConkey agar. The c.f.u. were manually counted the next day.

Deep thigh infection mouse model

Six-week-old female CD-1 mice (Charles River Laboratories) were rendered neutropenic by two intraperitoneal injections of cyclophosphamide (150 mg per kg (body weight)) 72 h apart[38,39]. One day later, 1×10^6 c.f.u. per ml of *A. baumannii* (ATCC 19606; in PBS) was injected into the right thigh. After 2 h, peptides (at MICs) or sterile water (control) were administered intraperitoneally. Mice were anesthetized with isoflurane before each procedure. Thigh muscles were excised on days 2 and 4 after infection, homogenized, serially diluted and plated on MacConkey agar, and c.f.u. were quantified. Experiments with six mice per group were blinded, and no animals were excluded. Data were analyzed using a one-way ANOVA with a Dunnett's test on $\log_{10}$-transformed values using GraphPad Prism (v10.4.2).

Circular dichroism spectroscopy

Circular dichroism spectra were recorded at 25 °C using Jasco J-815 and J-1500 spectropolarimeters with 1-mm quartz cuvettes. Peptides (20–50 µM) were analyzed in PBS, 1% *n*-dodecyl-β-d-maltoside, 60% trifluoroethanol in water (3:2, vol:vol), 50% methanol in water (1:1, vol/vol) or 10 mM SDS. Spectra were acquired from 195 to 260 nm (J-815: 1-nm bandwidth, 100 nm min^{-1}, ten accumulations; J-1500: 0.5-nm bandwidth, 50 nm min^{-1}, three accumulations). Data were background subtracted.

Calcein leakage (efflux) assay

Peptide-induced membrane permeabilization was assessed using calcein (622.5 Da)-loaded LUVs composed of POPC:POPG (1:1 mol/mol). PBS was prepared using 25 mM $NaH_2PO_4 \cdot H_2O$ and $Na_2HPO_4 \cdot 7H_2O$ (3:7 mol/mol), 100 mM NaCl and 1 mM EDTA, whereas calcein buffer was composed of 35 mM calcein, 25 mM $NaH_2PO_4 \cdot H_2O$ and $Na_2HPO_4 \cdot 7H_2O$ (3:7 mol/mol), 20 mM NaCl and 1 mM EDTA. Lipid films containing 1,1′-dioctadecyl-3,3,3′,3′-tetramethylindodicarbocyanine perchlorate (500:1 mol/mol) were hydrated in calcein buffer, subjected to ten freeze–thaw cycles, extruded (50 passes, 100-nm pores) and washed via size-exclusion chromatography. Peptides were added to 0.02 mM or 1 mM LUVs (P:L ratios from 1:100 to 1:10 and 1:2,000 to 1:500, respectively), and calcein release was monitored by fluorescence (λ_{ex}: 495 nm, λ_{em}: 520 nm) at 25 °C. Triton X-100 (10%) defined 100% leakage. Triplicate experiments were performed using a HORIBA Scientific Jobin Yvon FluoroLog-3 modular spectrofluorometer.

Dextran transport (influx/uptake) assay

POPC:POPG (1:1 mol/mol) GUVs containing biotinyl-phosphatidylethanolamine were prepared via electroswelling and immobilized on biotinyl-BSA-coated glass using streptavidin. GUVs (0.1 M sucrose) were incubated with an external solution (0.1 M glucose, 10 µM peptide, 100 mg ml^{-1} fluorescein isothiocyanate–dextran) at a P:L ratio of 1:50. Controls lacked peptides. GUVs were imaged after 60 min using a Zeiss Axio Observer.Z1 LSM 800 confocal microscope.

Channel electrical recordings

PLBs of DPhPC were formed using the Montal-Mueller method across a 100 µm Teflon aperture separating two chambers filled with 100 mM NaCl in PBS. DPhPC lipids (5 mg ml^{-1}) in pentane formed stable PLBs (~100 pF). Peptide-incubated LUVs (12–24 h, 37 °C, P:L ratio of 1:100) were added to the cis side (final peptide concentration = ~500 nM), and voltages (75–150 mV) were applied to induce pore insertion. Currents were recorded using pCLAMP 10.7, digitized using a Digidata 1440 A instrument connected to an Axopatch 200B amplifier and equipped with a CV 203BU headstage, with 50-kHz sampling (10-kHz Bessel filter) or 10-kHz sampling (2-kHz filter), and analyzed with Clampfit (v10.7.0.3) after digital low-pass Gaussian filtering (1 kHz).

Atomic force microscopy

SLBs of POPC:POPG (1:1) were formed on mica via the vesicle deposition method[71]. Lipid dissolution buffer contained 50 mM Tris-HCl and 50 mM KCl, and SLB buffer contained 50 mM Tris-HCl and 300 mM KCl. Extruded small unilamellar vesicles in SLB buffer with 5 mM $CaCl_2$ were used to prepare SLBs, followed by a 1-h incubation and ten gentle washes. Peptides were applied at a P:L ratio of 1:500, 1:250 or 1:100. Topographic imaging was performed using a Bruker Dimension Icon atomic force microscope controlled by NanoScope software (v10.30),

equipped with a PeakForce-HIRS-F-B silicon nitride probe operated in PeakForce quantitative nanomechanical mapping mode (spring constant: 0.12 N m^{-1}, 2 kHz, 25-nm amplitude, setpoint of <100 pN, 1-Hz scan). Images (512 samples per line) were processed in Gwyddion (v2.58) by flattening and plane fitting. SLB integrity was confirmed via force spectroscopy, and cross-sectional analysis was performed using NanoScope Analysis (v2.0) and Gwyddion (v2.58).

Design guidelines

- **Peptide length and amphipathic character:** peptides comprise 30 residues, with a central ~22-residue amphipathic segment forming a transmembrane α-helix. Non-polar residues (alanine, methionine, valine, leucine and isoleucine) compose the hydrophobic face; polar residues (threonine, glutamine, serine and asparagine) compose the hydrophilic face. Designs using strongly hydrophobic (leucine and isoleucine) and polar (glutamine and asparagine) residues show improved pore stability.
- **Salt bridges:** interpeptide salt bridges formed by oppositely charged residues (arginine/lysine and aspartic acid/glutamic acid) on the hydrophilic face are key for TBP stabilization. Designs encode either two (groups A and B) or four (groups C and D) salt bridges per peptide–peptide interface. Permissible salt bridge pairings include:
  - Group A:
    - First interface: 6–20 or 10–17
    - Second interface: 7–25 or 11–22
  - Group B:
    - First interface: 6–24 or 10–17
    - Second interface: 7–25 or 11–22
  - Groups C and D:
    - First interface: 6–17 or 6–20 or 6–21 or 6–24 paired with 10–17 or 10–20 or 10–21 or 10–24
    - Second interface: 7–22 or 7–25 paired with 11–22 or 11–25

  Each residue participates in only one salt bridge. Stability increases in the following order: 10–24 < 6–21 < 10–20 < 6–17 < 6–24 < 6–20 < 10–21 < 10–17 (first interface); 11–25 < 7–22 < 7–25 < 11–22 (second interface).
- **Aromatic stacking:** in designs with two salt bridges per interface, additional stabilization of TBP is provided by π–π interactions between aromatic residues (tryptophan and phenylalanine) on the hydrophobic face. Optimal positions are 13 and 15 for single stacking (groups A and C) and 8, 9, 20 and 26 for double stacking (groups B and D) per interface.
- **Peptide termini:** eight terminal residues are polar and can be tuned for function. Cationic termini stabilize transmembrane orientation. In groups A and B, avoid oppositely charged pairs at 6–2/3, 7–3/4, 24–27 and 25–28/29, which may form unintended interactions. N-terminal NH_3^+ and C-terminal COO^- favor antiparallel peptide arrangements. Peptide length can be modulated via the termini.

Reporting summary

Further information on research design is available in the Nature Portfolio Reporting Summary linked to this article.

Data availability

Data supporting the findings of this study are available in the article, Extended Data and Supplementary Information. Extended Data include in vitro leaky pore-forming activities, peptide design guidelines and designed sequence patterns. The Supplementary Information contains Supplementary Methods, Notes, Tables 1–14 and Supplementary Figs. 1–19, presenting simulated pore snapshots, interaction strengths, water density, permeation pathways, free energy profiles, antimicrobial activity, cytotoxicity, membrane depolarization and permeabilization, serum stability, animal studies, circular dichroism spectra, electrical recordings, AFM and fluorescence imaging. The Supplementary Materials include HPLC and MS certificates for all synthesized peptides. All simulation input and output files associated with this study are publicly available at Zenodo at https://doi.org/10.5281/zenodo.20171151 (ref. 72). Source data are provided with this paper.

Code availability

All simulation and associated analysis files necessary to reproduce this study have been deposited in Zenodo and are publicly available at https://doi.org/10.5281/zenodo.20171151 (ref. 72).

References

54. Abraham, M. J. et al. GROMACS: high performance molecular simulations through multi-level parallelism from laptops to supercomputers. *SoftwareX* **1–2**, 19–25 (2015).
55. Marrink, S. J., Risselada, H. J., Yefimov, S., Tieleman, D. P. & de Vries, A. H. The Martini force field: coarse grained model for biomolecular simulations. *J. Phys. Chem. B.* **111**, 7812–7824 (2007).
56. Qi, Y. et al. CHARMM-GUI Martini Maker for coarse-grained simulations with the Martini force field. *J. Chem. Theory Comput.* **11**, 4486–4494 (2015).
57. Torrie, G. M. & Valleau, J. P. Nonphysical sampling distributions in Monte Carlo free-energy estimation: umbrella sampling. *J. Comput. Phys.* **23**, 187–199 (1977).
58. Bussi, G., Donadio, D. & Parrinello, M. Canonical sampling through velocity rescaling. *J. Chem. Phys.* **126**, 014101 (2007).
59. Parrinello, M. & Rahman, A. Polymorphic transitions in single crystals: a new molecular dynamics method. *J. Appl. Phys.* **52**, 7182–7190 (1981).
60. Páll, S. & Hess, B. A flexible algorithm for calculating pair interactions on SIMD architectures. *Comput. Phys. Commun.* **184**, 2641–2650 (2013).
61. Tironi, I. G., Sperb, R., Smith, P. E. & van Gunsteren, W. F. A generalized reaction field method for molecular dynamics simulations. *J. Chem. Phys.* **102**, 5451–5459 (1995).
62. Hess, B., Bekker, H., Berendsen, H. J. C. & Fraaije, J. G. E. M. LINCS: a linear constraint solver for molecular simulations. *J. Comput. Chem.* **18**, 1463–1472 (1997).
63. Wassenaar, T. A., Pluhackova, K., Böckmann, R. A., Marrink, S. J. & Tieleman, D. P. Going backward: a flexible geometric approach to reverse transformation from coarse grained to atomistic models. *J. Chem. Theory Comput.* **10**, 676–690 (2014).
64. Lindorff-Larsen, K. et al. Improved side-chain torsion potentials for the Amber ff99SB protein force field. *Proteins* **78**, 1950–1958 (2010).
65. Jämbeck, J. P. M. & Lyubartsev, A. P. Derivation and systematic validation of a refined all-atom force field for phosphatidylcholine lipids. *J. Phys. Chem. B.* **116**, 3164–3179 (2012).
66. Jorgensen, W. L., Chandrasekhar, J., Madura, J. D., Impey, R. W. & Klein, M. L. Comparison of simple potential functions for simulating liquid water. *J. Chem. Phys.* **79**, 926–935 (1983).
67. Darden, T., York, D. & Pedersen, L. Particle mesh Ewald: an *N*·log(*N*) method for Ewald sums in large systems. *J. Chem. Phys.* **98**, 10089–10092 (1993).
68. Steinbach, P. J. & Brooks, B. R. New spherical-cutoff methods for long-range forces in macromolecular simulation. *J. Comput. Chem.* **15**, 667–683 (1994).
69. Humphrey, W., Dalke, A. & Schulten, K. VMD: visual molecular dynamics. *J. Mol. Graph.* **14**, 33–38 (1996).
70. Kumar, S., Rosenberg, J. M., Bouzida, D., Swendsen, R. H. & Kollman, P. A. The weighted histogram analysis method for free-energy calculations on biomolecules. I. The method. *J. Comput. Chem.* **13**, 1011–1021 (1992).

71. Richter, R. P. & Brisson, A. R. Following the formation of supported lipid bilayers on mica: a study combining AFM, QCM-D and ellipsometry. *Biophys. J.* **88**, 3422–3433 (2005).
72. Deb, R., & Vácha, R. Simulation and associated analysis files for paper 'Computational design of antimicrobial peptide nanopores'. *Zenodo* https://doi.org/10.5281/zenodo.20171151 (2026).

Acknowledgements

We thank M. Drabinová, A. Hánačková and T. Králová for their help with experiments; N. Labajová for helpful advice on SLB formation; G. Riddihough for assistance with manuscript writing; P. Jungwirth for careful reading of the manuscript and members of the laboratory of R.V. group for discussions. We thank M. Goulian from the University of Pennsylvania for kindly donating the following strains: *E. coli* AIC221 (*E. coli* MG1655 phnE_2::FRT (control strain for AIC222)) and *E. coli* AIC222 (*E. coli* MG1655 pmrA53 phnE_2::FRT (polymyxin resistant)). The scratch infection model was conducted in accordance with the regulations and guidelines of the Czech Animal Protection Act (246/1992), with approval from the Czech Ministry of Education, Youth and Sports of the Czech Republic (MEYS CR; MSMT-2963/2023-5) and the Institutional Animal Welfare Committee of the Faculty of Medicine and Dentistry, Palacký University Olomouc. Animal experiments performed at the University of Pennsylvania were reviewed and approved by the Institutional Animal Care and Use Committee of the University of Pennsylvania (University Laboratory Animal Resources; 806763 and 807055). Figures created using BioRender are attributed as such.

Author contributions

R.D. and R.V. conceived the project and designed the research. R.D. carried out simulations and analyzed data. I.K. contributed technical solutions to problems in simulations. R.D. and R.V. designed the peptides and developed the design guidelines. R.D. conducted calcein leakage assays with the assistance of I.K. R.D. and I.K. performed antimicrobial and hemolysis assays. R.D. and J.P. performed the AFM experiments. R.D. and E.V. performed channel electrical recordings. M.D.T.T. and C.d.l.F.-N. performed antimicrobial tests against ESKAPEE pathogens; cytotoxicity, serum stability, membrane permeabilization and depolarization assays; circular dichroism and mouse skin abscess and thigh infection models. K.D.B. and M.P. conducted the mouse scratch infection model. M.K. and G.B.N. performed the resistance evolution assay. R.D. analyzed experimental data with the assistance of I.K., M.D.T.T., J.P., E.V. and G.M. R.D. and R.V. wrote the paper with input from all authors.

Funding

This work was supported by the Czech Science Foundation (GA20-20152S), the European Research Council under the European Union's Horizon 2020 Research and Innovation program (101001470) and the National Institute of Virology and Bacteriology (Programme EXCELES, LX22NPO5103), funded by the European Union Next Generation EU. Additional support for the experiments was provided by the project 'Development of the System of Commercialization of Results at Masaryk University' (TG02010067), financed by the Technology Agency of the Czech Republic. Computational resources were provided by the Czech Education and Scientific Network (LM2015042) and the Central European Research Infrastructure Consortium Scientific Cloud (LM2015085), provided under the program 'Projects of Large Research, Development, and Innovations Infrastructures'. For AFM experiments, we acknowledge the Nanobiotechnology Core Facility and Instruct-CZ Centre, supported by MEYS CR (LM2023042 and LUC24105). For circular dichroism experiments, we acknowledge the CF Biomolecular Interactions and Crystallography facility of Czech Infrastructure for Integrative Structural Biology (CIISB), and Instruct-CZ Centre, supported by MEYS CR (LM2023042) and European Regional Development Fund-Project 'UP CIISB' (CZ.02.1.01/0.0/0.0/18_046/0015974). For fluorescence microscopy, we acknowledge Core Facility Cellular Imaging, supported by MEYS CR (LM2023050 Czech-BioImaging). C.d.l.F.-N. acknowledges funding from the National Institutes of Health (R35GM138201) and Defense Threat Reduction Agency (HDTRA1-21-1-0014). The resistance evolution experiments were funded by a grant from the Programme Johannes Amos Comenius under the MEYS CR (CZ.02.01.01/00/22_008/0004597). The mouse scratch infection model was additionally funded by the European Regional Development Fund (ENOCH, CZ.02.1.01/0.0/0.0/16_019/0000868) and the Czech MEYS CR through the European Advanced Translational Research Infrastructure in Medicine project (EATRIS-CZ, LM2023053).

Competing interests

The authors declare the following competing financial interests: R.D., I.K. and R.V. are inventors on a European Union patent application (EP4129319A1) filed by Masaryk University that covers the peptides and design guidelines described in this paper. C.d.l.F.-N. is a cofounder of and scientific advisor to Peptaris, provides consulting services to Invaio Sciences and is a member of the Scientific Advisory Boards of Nowture, Peptidus, European Biotech Venture Builder, the Peptide Drug Hunting Consortium, ePhective Therapeutics and Phare Bio. M.D.T.T. is a cofounder of and scientific advisor to Peptaris. The remaining authors declare no competing interests.

Additional information

Extended data is available for this paper at https://doi.org/10.1038/s41589-026-02269-z.

Supplementary information The online version contains supplementary material available at https://doi.org/10.1038/s41589-026-02269-z.

Correspondence and requests for materials should be addressed to Robert Vácha.

Peer review information *Nature Chemical Biology* thanks Seth Dickey, Ryuji Kawano and the other, anonymous, reviewer(s) for their contribution to the peer review of this work.

https://doi.org/10.1038/s41589-026-02269-z

Extended Data Table 1 | Sequence patterns

Group A One ST (13-13 on interface 1 and 15-15 on interface 2) and two SBs on each peptide-peptide interface				Group B Two STs (9-20/20-9 on interface 1 and 8-26/26-8 on interface 2) and two SBs on each peptide-peptide interface			
No.	SB		Sequence patterns	No.	SB		Sequence patterns
	Interface 1	Interface 2			Interface 1	Interface 2	
1	6-20	7-25	tttthbbhhpphspshpphapphpahtppt	17	6-24	7-25	tttthbbsspphhphhpphspphaaspppt
2	20-6	25-7	tppphaahhpphspshpphbpphpbhtttt	18	24-6	25-7	tppphaasspphhphhpphspphbbstttt
3	6/10-20	7/11-25	tttthbbhhbbhspshpphapphpahtppt	19	6/10-24	7/11-25	tttthbbssbbhhphhpphspphaaspppt
4	17/20-6	22/25-7	tppphaahhpphspshbphbpbhpbhtttt	20	17/24-6	22/25-7	tppphaasspphhphhbphspbhbbstttt
5	6-20	11-22	tttthbphhpbhspshpphapahpphtttt	21	6-24	11-22	tttthbpsspbhhphhpphspahapsptttt
6	20-6	22-11	tppthaphhpahspshpphbpbhpphtttt	22	24-6	22-11	tppthapsspahhphhpphspbhbpstttt
7	6/10-20	7/11-22	tttthbbhhbbhspshpphapahpphtttt	23	6/10-24	7/11-22	tttthbbssbbhhphhpphspahapsptttt
8	17/20-6	22/25-11	tppthaphhpahspshbphbpbhpbhtttt	24	17/24-6	22/25-11	tppthapsspahhphhbphspbhbbstttt
9	10-17	7-25	tttthpbhhbphspshaphhpphpahtppt	25	10-17	7-25	tttthpbssbphhphhaphspphpastppt
10	17-10	25-7	ttpphpahhaphspshbphhpphpbhtttt	26	17-10	25-7	ttpphpassaphhphhbphspphpbstttt
11	6/10-17	7/11-25	tttthbbhhbbhspshaphhpphpahtppt	27	6/10-17	7/11-25	tttthbbssbbhhphhaphspphpastppt
12	17/20-10	22/25-7	ttpphpahhaphspshbphbpbhpbhtttt	28	17/20-10	22/25-7	ttpphpassaphhphhbphspbhbbstttt
13	10-17	11-22	tttthpphhbbhspshaphhpahpphtttt	29	10-17	11-22	tttthppssbbhhphhaphspahppstttt
14	17-10	22-11	tttthpphhaahspshbphhpbhpphtttt	30	17-10	22-11	tttthppssaahhphhbphspbhppstttt
15	6/10-17	7/11-22	tttthbbhhbbhspshaphhpahpphtttt	31	6/10-17	7/11-22	tttthbbssbbhhphhaphspahppstttt
16	17/20-10	22/25-11	tttthpphhaahspshbphbpbhpbhtttt	32	17/20-10	22/25-11	tttthppssaahhphhbphspbhbbstttt
Group C **One ST (13-13 on interface 1 and 15-15 on interface 2) and four SBs on each peptide-peptide interface**				**Group D** **Two STs (9-20/20-9 on interface 1 and 8-26/26-8 on interface 2) and four SBs on each peptide-peptide interface**			
No.	**SB**		**Sequence patterns**	**No.**	**SB**		**Sequence patterns**
	Interface 1	**Interface 2**			**Interface 1**	**Interface 2**	
33	6/10-17/20	7/11-22/25	tttthbbhhbbhspshaphapahpahttttt	46	6/10-17/21	7/11-22/25	tttthbbssbbhhphhaphsaahpastttt
34	17/20-6/10	22/25-7/11	tttthaahhaahspshbphbpbhpbhtttt	47	17/21-6/10	22/25-7/11	tttthaassaahhphhbphsbbhpbstttt
35	6/10-17/21	7/11-22/25	tttthbbhhbbhspshaphhaahpahttttt	48	6/10-17/24	7/11-22/25	tttthbbssbbhhphhaphspahaastttt
36	17/21-6/10	22/25-7/11	tttthaahhaahspshbphhbbhpbhtttt	49	17/24-6/10	22/25-7/11	tttthaassaahhphhbphspbhbbstttt
37	6/10-17/24	7/11-22/25	tttthbbhhbbhspshaphhpahaahtttt	50	6/10-21/24	7/11-22/25	tttthbbssbbhhphhpphsaahaastttt
38	17/24-6/10	22/25-7/11	tttthaahhaahspshbphhpbhbbhtttt	51	21/24-6/10	22/25-7/11	tttthaassaahhphhpphsbbhbbstttt
39	6/10-20/21	7/11-22/25	tttthbbhhbbhspshpphaaahpahttttt	52	17/21/24-6/10	22/25-7/11	tttthaassaahhphhbphsbbhbbstttt
40	20/21-6/10	22/25-7/11	tttthaahhaahspshpphbbbhpbhtttt				
41	6/10-20/24	7/11-22/25	tttthbbhhbbhspshpphapahaahtttt				
42	20/24-6/10	22/25-7/11	tttthaahhaahspshpphbpbhbbhtttt				
43	6/10-21/24	7/11-22/25	tttthbbhhbbhspshpphhaahaahtttt				
44	21/24-6/10	22/25-7/11	tttthaahhaahspshpphhbbhbbhtttt				
45	17/20/21/24-6/10	22/25-7/11	tttthaahhaahspshbphbbbhbbhtttt				

Peptide sequence patterns (30 residues in length), designed using our guidelines, are grouped (A–D) by the total number of aromatic π–π stacking (ST) and salt bridge (SB) interactions per peptide–peptide interface in TBP. Patterns comprise polar (**p**: Q/N/T/S), hydrophobic (**h**: L/I/A/M/V), basic (**b**: R/K, blue), acidic (**a**: D/E, red), aromatic (**s**: W/F, silver) and terminal (**t**) residues. SBs (or p substitutions) are annotated (for example, '17/21/24–6/10' in pattern 52 denotes b–a interactions at these positions in the first interface). Pairs of patterns separated by long lines differ only by swapped SB partners; in A and B, short lines indicate variants with extra b residues on the polar face to enhance net charge. Aromatic residues mediate STs (or h substitutions). Terminal residues can be p or b.

https://doi.org/10.1038/s41589-026-02269-z

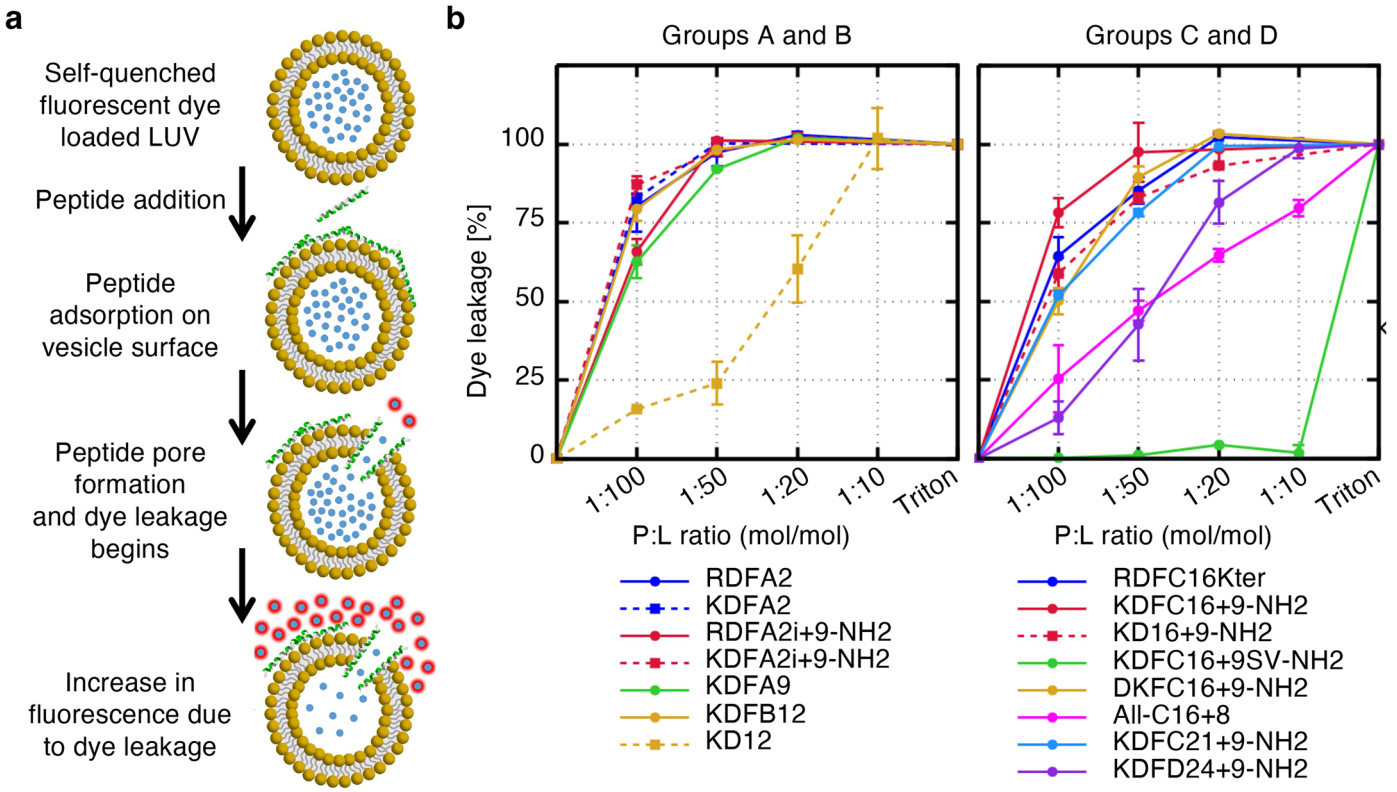

Extended Data Fig. 1 | *In vitro* leaky pore-forming activity. a, Schematic of liposome-encapsulated calcein leakage via peptide pore formation. **b**, Calcein release from POPC:POPG (1:1) LUVs as a function of P:L ratio. Triton X-100 induced 100% leakage. Of the 22 peptides synthesized, 15 were soluble in PBS; 14 induced concentration-dependent dye leakage; only KDFC16 + 9SV-NH2 showed none, likely due to narrow pores observed in simulations; strong agreement between leakage assay and MD predictions. Experiments were performed in triplicate. Data are presented as mean ± s.d.

https://doi.org/10.1038/s41589-026-02269-z

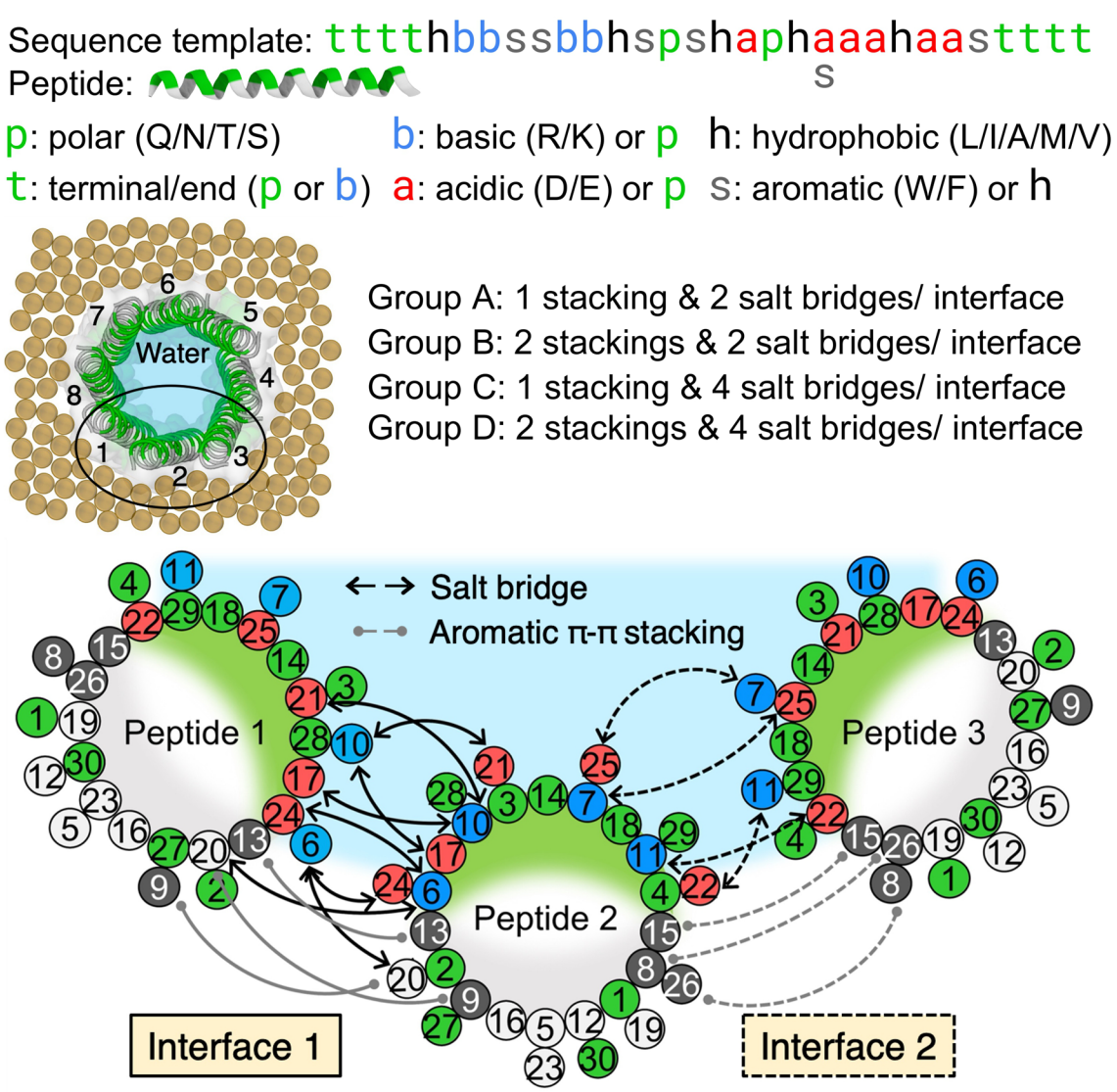

Extended Data Fig. 2 | Design guidelines. A peptide sequence template of 30 amino acids in length (central hydrophobic patch spanning ~22 residues), defined by identifiers - p, h, b, a, s, and t - characterizing specific amino acids. Sequence templates are categorized into four groups (A, B, C, D) based on the total number and type of interactions that can be designed at each interface. Schematic of aromatic π-π stacking and salt bridge interactions shown between three antiparallel neighboring transmembrane peptides (shown in helical wheels at the bottom) representing two peptide–peptide interfaces of an octameric TBP. Color coding: peptide hydrophilic and hydrophobic residues/ patches in green and white; basic and acidic residues in blue and red; and aromatic residues in silver.

nature portfolio

Corresponding author(s): Robert Vácha

Last updated by author(s): May 5, 2026

Reporting Summary

Nature Portfolio wishes to improve the reproducibility of the work that we publish. This form provides structure for consistency and transparency in reporting. For further information on Nature Portfolio policies, see our Editorial Policies and the Editorial Policy Checklist.

Statistics

For all statistical analyses, confirm that the following items are present in the figure legend, table legend, main text, or Methods section.

n/a	Confirmed
☐	☒ The exact sample size (*n*) for each experimental group/condition, given as a discrete number and unit of measurement
☒	☐ A statement on whether measurements were taken from distinct samples or whether the same sample was measured repeatedly
☐	☒ The statistical test(s) used AND whether they are one- or two-sided *Only common tests should be described solely by name; describe more complex techniques in the Methods section.*
☒	☐ A description of all covariates tested
☐	☒ A description of any assumptions or corrections, such as tests of normality and adjustment for multiple comparisons
☐	☒ A full description of the statistical parameters including central tendency (e.g. means) or other basic estimates (e.g. regression coefficient) AND variation (e.g. standard deviation) or associated estimates of uncertainty (e.g. confidence intervals)
☐	☒ For null hypothesis testing, the test statistic (e.g. *F*, *t*, *r*) with confidence intervals, effect sizes, degrees of freedom and *P* value noted *Give P values as exact values whenever suitable.*
☒	☐ For Bayesian analysis, information on the choice of priors and Markov chain Monte Carlo settings
☒	☐ For hierarchical and complex designs, identification of the appropriate level for tests and full reporting of outcomes
☒	☐ Estimates of effect sizes (e.g. Cohen's *d*, Pearson's *r*), indicating how they were calculated

Our web collection on statistics for biologists contains articles on many of the points above.

Software and code

Policy information about availability of computer code

Data collection	MD simulations were performed using GROMACS (v5.1.4 for coarse-grained and v2021.4 for all-atom simulations). Peptide structures were built in PyMOL and converted using martinize.py. Lipid bilayers were constructed using CHARMM-GUI Martini Maker (accessed YYYY). Coarse-grained systems were back-mapped using initram.sh. Electrophysiology data were acquired using pCLAMP (v10.7). AFM data were acquired using Bruker NanoScope (v10.30).
Data analysis	Simulation trajectories were analyzed using VMD. Pore radius and permeation pathways were calculated using HOLE. Umbrella sampling data were analyzed using WHAM. Electrophysiology data were analyzed using Clampfit (v10.7.0.3). Statistical analyses were performed using GraphPad Prism (v10.4.2). AFM images were analyzed using Gwyddion (v2.58), and force spectroscopy data were analyzed using NanoScope Analysis (v2.0).

For manuscripts utilizing custom algorithms or software that are central to the research but not yet described in published literature, software must be made available to editors and reviewers. We strongly encourage code deposition in a community repository (e.g. GitHub). See the Nature Portfolio guidelines for submitting code & software for further information.

Data

Policy information about availability of data

All manuscripts must include a data availability statement. This statement should provide the following information, where applicable:

- Accession codes, unique identifiers, or web links for publicly available datasets
- A description of any restrictions on data availability
- For clinical datasets or third party data, please ensure that the statement adheres to our policy

Data supporting the findings of this study are available in the Article, Extended Data, and Supplementary Information. Extended Data include in vitro leaky pore-forming activities, peptide design guidelines, and designed sequence patterns. The Supplementary Information contains Supplementary Methods, Supplementary Note, Supplementary Tables S1–S14, and Supplementary Figures S1–S19 presenting simulated pore snapshots, interaction strengths, water density, permeation pathways, free energy profiles, antimicrobial activity, cytotoxicity, membrane depolarization and permeabilization, serum stability, animal studies, CD spectra, electrical recordings, AFM, fluorescence imaging, and Supplementary Materials including HPLC and mass spectrometry certificates of all synthesized peptides. Source data used to generate Figs. 1–5 and Extended Data Fig. 1 are provided with this paper. All simulation input and output files associated with this study are publicly available at Zenodo (DOI: 10.5281/zenodo.11026320) (ref. 72).

Research involving human participants, their data, or biological material

Policy information about studies with human participants or human data. See also policy information about sex, gender (identity/presentation), and sexual orientation and race, ethnicity and racism.

Reporting on sex and gender	N/A
Reporting on race, ethnicity, or other socially relevant groupings	N/A
Population characteristics	N/A
Recruitment	N/A
Ethics oversight	N/A

Note that full information on the approval of the study protocol must also be provided in the manuscript.

Field-specific reporting

Please select the one below that is the best fit for your research. If you are not sure, read the appropriate sections before making your selection.

☒ Life sciences ☐ Behavioural & social sciences ☐ Ecological, evolutionary & environmental sciences

For a reference copy of the document with all sections, see nature.com/documents/nr-reporting-summary-flat.pdf

Life sciences study design

All studies must disclose on these points even when the disclosure is negative.

Sample size	For animal experiments, sample sizes were determined based on previous studies using similar infection models (https://doi.org/10.1038/s41551-021-00801-1, https://doi.org/10.1038/s41551-024-01201-x, https://doi.org/10.1038/s41564-025-02061-0). For all other experiments, no formal statistical method was used to predetermine sample size; instead, sample sizes were chosen based on standard practice in the field and were sufficient to ensure reproducibility and consistency of the results across independent replicates.
Data exclusions	No data was excluded.
Replication	Experiments were performed with at least three independent replicates where applicable. All attempts at replication were successful.
Randomization	For animal experiments, mice were randomly allocated to experimental groups. For in vitro assays and simulations, randomization was not applied as experiments were conducted under predefined conditions with objective quantitative measurements.
Blinding	Peptides were solubilized and labelled with internal codes to ensure unbiased experimentation. For animal infection models, investigators were blinded to group allocation during data collection and analysis. For in vitro assays and simulations, blinding was not applicable due to the objective and automated nature of the measurements.

Reporting for specific materials, systems and methods

We require information from authors about some types of materials, experimental systems and methods used in many studies. Here, indicate whether each material, system or method listed is relevant to your study. If you are not sure if a list item applies to your research, read the appropriate section before selecting a response.

Materials & experimental systems

n/a	Involved in the study
☒	☐ Antibodies
☐	☒ Eukaryotic cell lines
☒	☐ Palaeontology and archaeology
☐	☒ Animals and other organisms
☒	☐ Clinical data
☒	☐ Dual use research of concern
☒	☐ Plants

Methods

n/a	Involved in the study
☒	☐ ChIP-seq
☒	☐ Flow cytometry
☒	☐ MRI-based neuroimaging

Eukaryotic cell lines

Policy information about cell lines and Sex and Gender in Research

Cell line source(s)	Human embryonic kidney cells (HEK293T) were obtained from the American Type Culture Collection (ATCC; CRL-3216). Cytotoxicity assays on human dermal fibroblasts (HDFs) were performed as a service by Essence Line (Czech Republic) at Sterlab (France) using a Neutral Red Uptake assay. Human red blood cells (hRBCs; type A–, male donor) and human serum were purchased from Zen-Bio.
Authentication	None of the cell lines used were authenticated.
Mycoplasma contamination	The cell lines were not tested for mycoplasma contamination.
Commonly misidentified lines (See ICLAC register)	No commonly misidentified cell lines were used.

Animals and other research organisms

Policy information about studies involving animals; ARRIVE guidelines recommended for reporting animal research, and Sex and Gender in Research

Laboratory animals	CD-1 mice (Mus musculus; outbred ICR/CD-1 genetic background; 6-week-old females; Charles River Laboratories, stock no. 18679700-022) and Balb/c mice (Mus musculus; inbred strain; 8–10-week-old females; Anlab/Inotiv) were used. Mice were housed under a 12 h light/dark cycle at 22 °C and 50% humidity (CD-1 models) or 20–24 °C and 40–70% humidity (Balb/c scratch model).
Wild animals	No wild animals were used in this study.
Reporting on sex	All animals used in the experiments were female.
Field-collected samples	No field-collected samples were used in this study.
Ethics oversight	The animal protocols for the skin abscess infection model (806763) and the thigh infection model (807055) were reviewed and approved by the Institutional Animal Care and Use Committee (IACUC) of the University of Pennsylvania (University Laboratory Animal Resources, ULAR). The scratch infection model was conducted in accordance with the Czech Animal Protection Act (No. 246/1992) and approved by the Czech Ministry of Education, Youth, and Sports (MSMT-2963/2023-5) and the Institutional Animal Welfare Committee of the Faculty of Medicine and Dentistry, Palacký University Olomouc.

Note that full information on the approval of the study protocol must also be provided in the manuscript.

Plants

Seed stocks	N/A
Novel plant genotypes	N/A
Authentication	N/A